Improving image quality of synthetically zoomed tomographic images

Thesis submitted in partial fulfillment

of the requirements for the degree of

Master of Science (by Research)

in

Communication system and signal processing

by

Neha Dixit

200636002

nehadixit@research.iiit.ac.in

International Institute of Information Technology

Hyderabad, India

March 2012

INTERNATIONAL INSTITUTE OF INFORMATION TECHNOLOGY

Hyderabad, India

CERTIFICATE

It is certified that the work contained in this thesis, titled "Improving image quality of synthetically zoomed tomographic images" by Neha Dixit, has been carried out under my supervision and is not submitted elsewhere for a degree.

Date

Advisor: Prof. Jayanthi Sivaswamy

To my guide and my parents,
for believing in me and supporting me in hard times.

Acknowledgments

I most sincerely express my gratitude to Dr. Jayanthi Sivaswamy for her guidance and vision which has led to the realization of this thesis. She has not only been the mentor for this work but also a role model for me in the research domain. I thank my husband Nihar and friends Guru, Sai, Sandeep and Yogi for their moral support and companionship during this part of my life.

Abstract

3-D medical images such as Computed Tomography(CT), Positron Emission Tomography(PET) and Magnetic Resonance Imaging(MRI) are commonly used for diagnosis. Tomographic reconstruction is the underlying technique for all these images. It is often of interest to increase the resolution of these images. Some of the possible solutions for increasing the resolution are: increasing the number of detectors, changing the detector material/geometry, increasing the excitation energy level or scanning time. These solutions are limited in terms of practical implementation. Hence, finding solutions at the processing level (post data acquisition) is of interest. This thesis focuses on the problem of preserving details and quality of tomographic images after upsampling. We have explored two different approaches for generating higher resolution images. These are based on re-examining the lattice geometry for reconstruction. We offer two novel solutions, one which uses a hexagonal instead of the conventional square lattice and a second one based super resolution strategy which combines samples drawn from two lattices.

In the first solution, we reconstruct the image onto a hexagonal lattice. These samples are then interpolated to find the samples on the desired higher resolution square lattice. In the super resolution (SR)- based solution we reconstruct the images onto 2 low resolution lattices. The lattices are rotated versions of each other which provide a 'different view' of an object/scene. For generating low resolution images both square and hexagonal sampling have been considered.

The two solutions have been implemented and tested using a variety of test objects. These objects which are called phantoms were chosen to be of 2 types: analytical and real.

Three analytically generated phantoms used were Concentric rings, dots and lines. *Two* real PET phantoms were Nema and Hoffman Brain phantoms. The results were benchmarked against upsampled images generated by: Direct upsampling and an existing super resolution technique which uses Union of Shifted Lattice (USL) samples. The evaluation results show a qualitative and quantitative improvement over results obtained by direct upsampling. The SR-based results are comparable to that obtained with USL in quality. However, the main strength of the proposed SR-based solution is the computational savings and a reduced number of required images for a given upsampling factor.

Contents

List of Figures

List of Tables

Chapter 1

Introduction

The goal of medical imaging is to provide a method to visualize the interior of the human body at micro (cellular) to macro (organ) level. These images are used for studying the anatomy of the human body for diagnosing functional status of an organ; to inspect for the presence of tumor, lesion, cancer, broken bone, ruptured vessel etc. Some of the well known imaging modalities are X-ray, magnetic resonance, ultrasound, positron emission tomography etc. These modalities use different physical excitation like X rays, gamma rays or photons, magnetic field, etc. to generate the image.

Tomography is a widely used imaging technique for visualizing the cross-sectional structure of a body. Figure 1.1 explains the concepts of tomography, where slices S1 and S2 are cross-sectional images (of some thickness) of the given volumetric data. Tomographic images are generated from a set of one-dimensional projection data known as a *sinogram*. A sinogram is generated by projecting an object at different angles around a single axis. It is discrete function radial (r) and angular (θ) variables. Images are reconstructed from this data using a "Reconstruction algorithm" like filtered back projection, algebraic reconstruction etc. Resolution and quality of reconstructed images depends on the number of projections (r) and angular (θ) samples. The three dimensional structure of the body/ob-

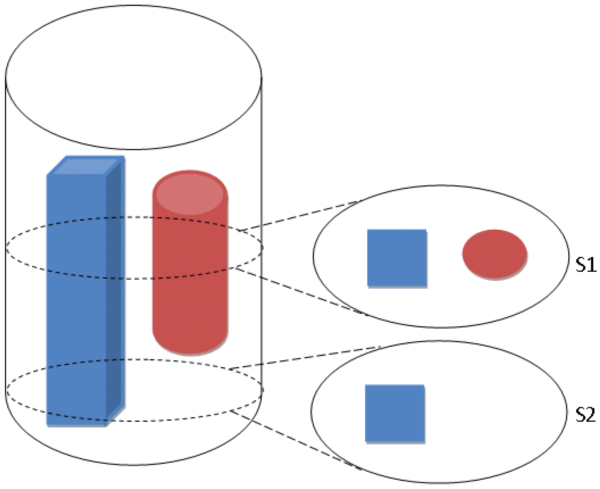

Figure 1.1: Tomography concept

ject can be generated directly from sinogram data (of the whole object) or by rendering the cross-sectional images.

1.1 Types of Tomography

Tomographic images differ based on the physics involved in acquiring the sinogram data. Some of the well known tomographic modalities are :

1.1.1 X-ray computed tomography

X-ray computed tomography (CT) sometimes called computed axial tomography (CAT) uses X-rays for imaging body. In CT scan, X-ray source and X-ray detectors rotate around the body measuring the amount of radiation being absorbed by the body. Typical size of the acquired CT image is 512×512.

1.1.2 Nuclear imaging

Nuclear imaging is used to visualize the structure and *function* of an organ, tissue, bone or system of the body. In nuclear imaging, radioactive materials called radio pharmaceuticals or radiotracers are either injected or injested. Radiotracers eventually decay by emitting photons. Sinogram data is generated by detecting the energy of the emitted photons (gamma rays) using a gamma camera. Two well known nuclear imaging modalities are: SPECT (single photon emission computed tomography) and PET (positron emission tomography). In SPECT, the radiotracer emits a single photon (while decaying) which is directly captured by a gamma camera but in the case of PET, the radiotracer emits a positron which collides with an electron and produces two photons which are simultaneously detected by two gamma cameras at opposite sides of the body. The typical size of a image in this modality is 128×128.

1.1.3 Magnetic resonance imaging

Magnetic resonance imaging (MRI) was originally known as nuclear magnetic resonance (NMR) imaging which originated in physics. Detailed MR images allow physicians to better visualise soft tissues and evaluate various parts of the body and certain diseases that may not be assessed adequately with other imaging methods such as X-ray, ultrasound or computed tomography. Imaging is done by generating a strong magnetic field of the order of 1-9 Tesla for humans and around 21 Tesla for animals. The generated magnetic field is used to polarize and excite hydrogen nuclei in the water molecule in the human body. This polarization produces a detectable signal which is spatially encoded using RF receiver or antenna. The typical size of MR image is 256×256.

1.1.4 Electron tomography

Electron Tomography (ET) is a technique for obtaining detailed 3D structures of sub cellular macromolecular objects. Sinogram generation is similar to that of CT. In this process, an electron source and detectors are rotated about the center of the target sample. The collected information is then used to assemble a three dimensional image of the target.

1.1.5 Atom probe tomography

Atom probe tomography (APT) is used in material sciences to determine the positions of atoms in an object with atomic precision using a position sensitive detector. It is not widely used in medical imaging.

1.2 Limitations of Tomography

Quality of an image means clarity and detail it holds, and it can be quantified by
a) its signal to noise ratio (SNR), and
b) resolution i.e. how clearly it can resolve two very closely spaced lines
The resolution of tomographic images is partly limited by the width of detector, which means that a tomographic equipment cannot distinguish between the object placed at a distance less than the spacing of detector width. In the case of nuclear imaging, signal production is stochastic in nature and due to limited radiotracer dosage (low) the acquired sinogram data is characterized by fairly low signal to noise ratio which results in poor image quality.
The resolution and quality of such images can be improved by increasing the number of detectors, number of angular views and radiotracer dosages. These options however are not practical: the number of detectors are limited by detector size and spatial constraints. Increasing the angular views increases the scanning time (prolong exposure to radiation) which, in turn, increases the probability of patient movement thus introducing motion artifacts. In-

creasing the percentage intake of radiotracer is theoretically a solution but practically not, because it is hazardous for patient. The only available option is thus to address the problem at the reconstruction stage. This can help in improving the quality of images which are being generated by a system without changing the hardware or dosage protocol. In this thesis, we investigate methods to improve the quality of reconstructed images. The main objective is to increase the quality and resolution of a tomographic image while not compromising its quality.

1.3 Proposed Solution

A common solution to improve the resolution of an image is to upsample or zoom. Zooming or upsampling is done by interpolating the data/image which leads to loss of details and smoothing of image. This is not advisable because it further deteriorates the quality of resulting (upsampled) image and can introduces some artifacts which can sometimes lead to faulty diagnoses. To address the aforementioned issues, we propose two non-trivial solutions which improves the quality of the upsampled image.

a) **Hexagonal lattice (Single lattice approach)**: Due to hardware limitation the image generated via reconstruction from a sinogram is always defined on square lattice. Since a sinogram contains information about a continuous structure we can back project it onto any lattice. Instead of square sampling we consider hexagonal sampling for reconstructing the initial images. In the proposed solution, upsampled image is generated from an image defined on hexagonal lattice.

b)**Super resolution (Multiple lattice approach**: Super resolution is a technique that enhances the resolution of an image by combining several low resolution images. These low resolution images contain different information about the same object/scene. The proposed solution tries to improve the resolution of tomographic images by combining two low resolution images which are rotated version of each other. In this approach the given sinogram is back projected onto square(hexagonal) lattice and its rotated version. Next, an upsampled image is generated by combining information from these low resolution images.

1.3.1 Organization of thesis

Chapter 2 begins with a brief background about various tomography techniques followed by the ongoing work in research community that is relevant to our work. Chapter 3 present our motivations and driving force for the approaches being considered. Chapter 4 gives detailed explanation with mathematical framework about the two approaches, followed by the implementation details. Chapter 5 includes phantoms and quality metrics used by us in validating our method with the existing one. Chapter 6 contains the consolidated evaluation of our techniques presented in chapters 4. We have also given our comments on observed results in this chapter. Chapter 7 summarizes our work and provides some of the future directions that this research can grow into, and concludes the thesis.

Chapter 2

Tomography: An Overview

Centuries ago dissection was the only option to study the human anatomy for diagnostic purposes. However it was possible only in the postmortem. As science progressed, by early 19th century, endoscopy was the first in vivo imaging technique developed by Philip Bozzini. It involved an instrument used to examine the interior of a hollow organ or cavity of the body by inserting directly into the organ. The main disadvantage of this technique is that it can be used only in the body cavity and not inside an organ without risking infection, punctured organs and over sedations. Later on the accidental discovery of the X-rays by Roentgen, enabled noninvasive *in vivo* imaging of human body. However it had its own disadvantages like inability to highlight anything other than bones and inability to generate cross-sectional images. Development of tomography made it possible to view 3D and *cross sectional* view of any object.

2.1 Data Acquisition by Different Modalities

Different tomographic modalities use different physical phenomena for generating data from which image is generated or reconstructed. The collected data basically represents attenuation profile of photons traversing through the object/body.. In this study, only two types of

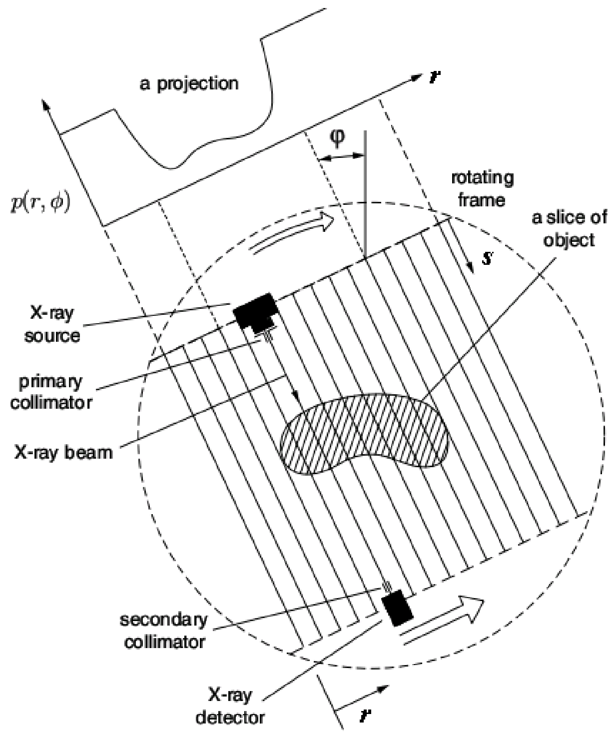

Figure 2.1: Principle of measurement of projections in CT.(source [23])

modalities are looked at: Computed Tomography (CT) and PET(positron emission tomography).

2.1.1 Computed tomography

Characteristics of the internal structure of an object such as dimensions, shape, internal defects and density are readily available from computed tomographic images.

In computed tomography, an object is placed between a X-ray source (or sources) and a series of detectors which are placed in either planar or cylindrical geometric arrangement. For generating the data a narrow beam of X-ray is passed through the body from the source to the detector. Figure 2.1 shows the geometry of a CT scanner with parallel beam generated by an X-ray source moving along a line. The resulting 1-D data acquired by the detector is shown as $p_\phi(r)$ where r is the distance and ϕ is the angle of the beam. Similar kinds of profiles are obtained by varying ϕ or rotating the source-detector pair around a common axis. These profiles constitute as a sinogram. Figure 2.1 shows a 1_st generation CT scanner geometry which uses a single pair of source and detector. The main disadvantage of this scanner was high dosage and long scan time. In the present scenario, CT systems use thin wide fan beam covering the entire slice of the object. It reduces the scan time and dosage by a considerable amount. In fan beam geometry, a divergent X-ray source is present at one end and curved detector array at other end. During image reconstruction the fan beam data is re-binned (interpolate) to parallel data geometry.

2.1.2 Positron emission tomography

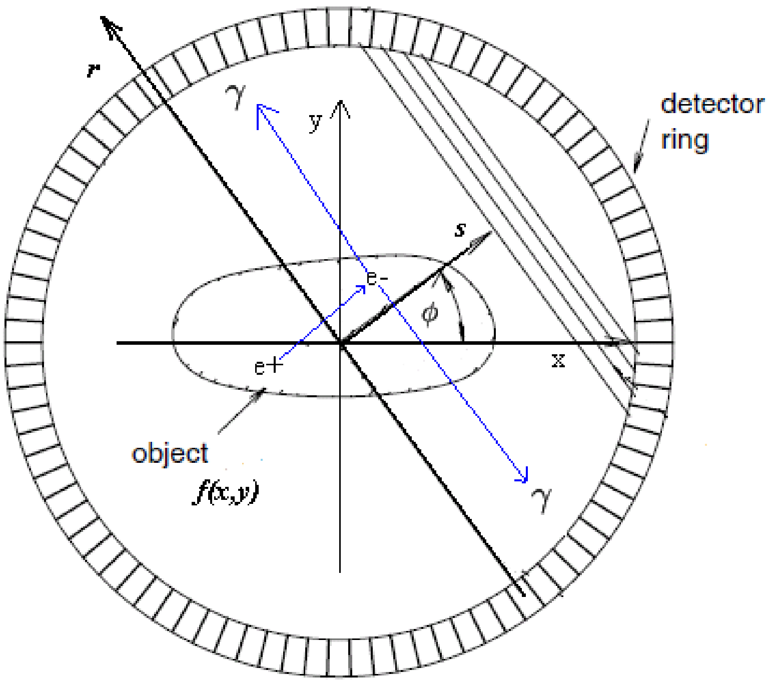

Figure 2.2: Principle of measurement of projections in PET, where e^+ and e^- represent positron and electorn; γ represents a photon.(source[23])

Nuclear tomography is a diagnostic imaging technique used to study the metabolic activity of cells in human body. During the imaging process, a small amount of radioactive materials called radio pharmaceuticals or radio tracers are introduced in human body. These materials accumulate inside the body depending on the metabolic activity of the region. An abnormal increase in the concentration of radio tracer in a tissue indicates the presence of malignant tumor cells or clot or blockage in blood vessels. In PET, radiotracer decays by emitting positron (e+ antimatter) which eventually collides with electron (e-) and they annihilate producing high energy (511Kev) photons (γ rays) travelling in two opposite direction. Data is generated by capturing the photon pair using gamma cameras arranged in a concentric ring geometry. Figure 2.2 shows the PET scanner geometry and electron positron annihilation.

2.2 Radon Transform (Sinogram or Projection data)

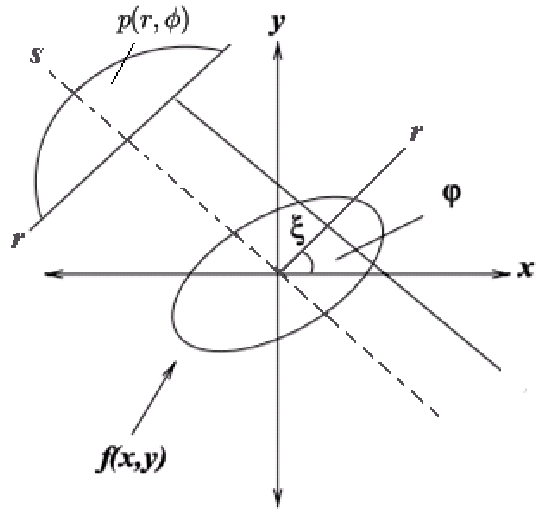

Figure 2.3: f(x,y) represents a function defined on square coordinate (x,y) and $p(r, \phi)$ is 1-D sinogram of f(x,y) defined over rotated (r,s) coordinate system

All tomographic modalities use Radon transform as the basic principle for generating the cross-sectional images. The mathematical foundation was laid down by Johann Radon. Radon transform is an integral transform consisting of the integral of a function over straight line [23].

The Radon transform (RT) of a distribution f(x, y) (Fig.2.3) is given as

$$p_\phi(r) = R(f(x,y)) = \int_{-\infty}^{+\infty}\int_{-\infty}^{+\infty} f(x,y)\delta(x\cos\phi + y\sin\phi - r)dxdy \tag{2.1}$$

Here $p_\phi(r)$ is the integral of function f(x,y) for all x and y which satisfy the equation $(x\cos\phi + y\sin\phi - r) = 0$, where r is the perpendicular distance of a line from origin.

These 1-D Radon transform can be interpreted as projection of function f(x,y) at an angle ϕ onto the axis s at some discrete r values. The coordinate (r, s) are related to (x, y) by a rotational matrix (Eqns 2.2,2.3)

$$\begin{bmatrix} r \\ s \end{bmatrix} = \begin{bmatrix} \cos\phi & \sin\phi \\ -\sin\phi & \cos\phi \end{bmatrix} \begin{bmatrix} x \\ y \end{bmatrix} \tag{2.2}$$

$$\begin{bmatrix} x \\ y \end{bmatrix} = \begin{bmatrix} \cos\phi & -\sin\phi \\ \sin\phi & \cos\phi \end{bmatrix} \begin{bmatrix} r \\ s \end{bmatrix} \tag{2.3}$$

writing Eqn2.1 in terms of Eqn2.2

$$p_\phi(r) = R(f(x,y)) = \int_{-\infty}^{+\infty} f(r\cos\phi - s\sin\phi, r\sin\phi + s\cos\phi)ds \tag{2.4}$$

Combination of such 1-dimensional Radon transform or projections for different ϕ is called as SINOGRAM, because the Radon transform (for different angles) of an impulse function is a sine wave. Hence, the sinogram of any object appears graphically as a superimposition of sine waves with different amplitudes and phases.

For practical purposes the projection data $p(r, \phi)$ is a mapping from continuous f(x,y) to a discrete function $p(r, \phi)$ where, r is the number of projections and ϕ is the number of angles.

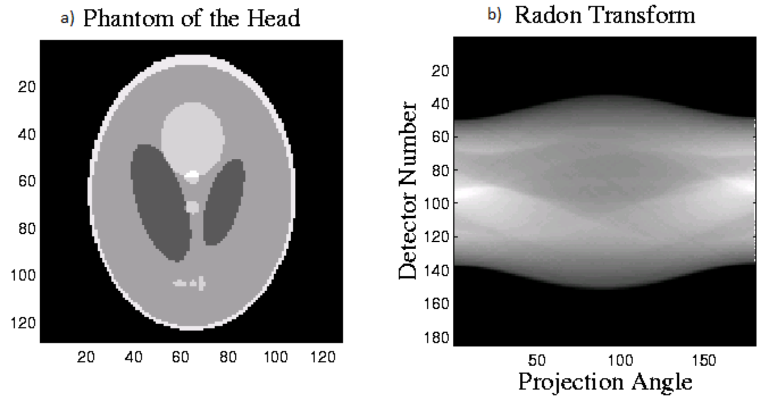

Figure 2.4: (a) Shepp-Logan brain phantom (b) the sinogram $p(r, \phi)$ of (a) with 180 discrete radial and angular samples.

2.3 Tomographic Image Reconstruction

Image reconstruction is an inverse problem associated with tomography [38] where for a given $p(r, \phi)$, one is interested in recovering $f(x, y)$. We can reconstruct the desired cross-sectional image by backprojecting (smearing) $p(r, \phi)$ on the points (x,y) which satisfies the equation $(x\cos\phi + y\sin\phi - r) = 0$. This is repeated for all the angles ϕ ranging from 0 to π. Eqn.2.5 describes the procedure of backprojection.

$$b(x, y) = B(p(r, \phi)) = \int_0^\pi p(x\cos\phi + y\sin\phi, \phi)d\phi \tag{2.5}$$

Since in a practical implementation, the sinogram data is discretized and images are reconstructed onto discrete square lattice. Discrete version of eqn.2.5 is given as:

$$b(x_i, y_j) = B(p(nr, m\phi)) = \sum_0^{M-1} p(x_i\cos(\frac{m\pi}{M-1}) + y_j\sin(\frac{m\pi}{M-1})) \tag{2.6}$$

Reconstructing images by direct backprojection is not a wise option since it introduces distrotion. The backprojection result for Shepp-Logan phantom is shown in Figure 2.5(c). The reconstructed (via backprojection) image is blurred and appears to be washed out visually when compared to the original image. This blurring is because of Point Spread

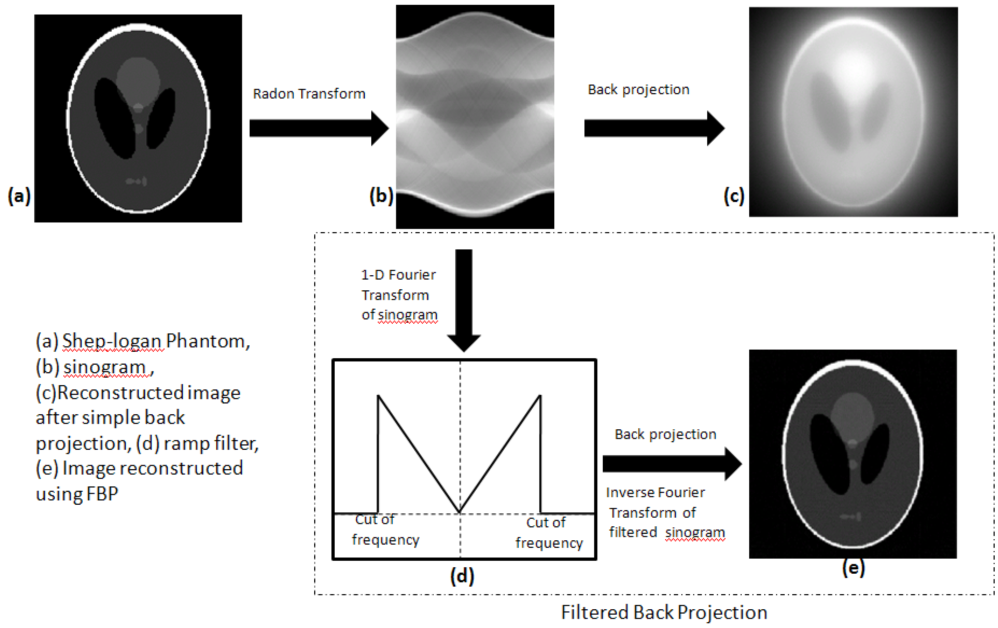

Figure 2.5: Pipeline

Function (PSF) which gives more emphasis to low frequencies as compare to high frequencies. function $\frac{1}{\sqrt{x^2+y^2}}$ and can be explained through the given relation in [22]

$$b(x,y) = \frac{1}{\sqrt{x^2+y^2}} \otimes f(x,y) \tag{2.7}$$

In polar coordinate the above equation is written as

$$b(r,\phi) = \frac{1}{|r|} \otimes f(r,\phi) \tag{2.8}$$

To overcome or minimize the above problem a well known algorithm Filtered backprojection (FBP) is being used generally to reconstruct the images. This frequency domain algorithm is based on popular Fourier slice theorem which states that the one dimensional spectrum $P_\phi(w)$ of a projection $p_\phi(r)$ obtained from the function f(x,y) is equal to the central slice at the angle ϕ of the two dimensional image spectrum F(u,v).

FBP algorithm

a) Take 1-D fourier transform of the sinogram data $p(r,\phi)$ for every view angle ϕ. Let this be denoted as $P_\phi(w)$.

b) Since convolution is equivalent to multiplication in fourier domain, so 1-D fourier transform is multiplied with 1-D ramp ($|w|$) filter function to nullify the effect of PSF.
c) The filtered sinogram which is in the frequeny domain is then transformed back to spatial domain by taking the 1-D inverse fourier tranform.
d) The final image (defined on sq lattice) is generated by back projecting the processed sinogram.

Fig.2.5 (e)Shows that FBP pipeline. The results of FBP preserves details when compared to back projected image Fig.2.5(c).

In the case of PET, the strength of the detected signal (projection or sinogram data) is very weak which results in a low resolution (typically 128×128) recon image. There is also a decrease in SNR in the reconstructed image [23]. Iterative reconstruction algorithms are more suited for such types of data rather than FBP. One of the most popular iterative reconstruction algorithm is Maximum Likelihood based. It is based on Bayesian approach and assumes that reconstructed image matrix x is computed from measured sinogram matrix y [38]. Then according to Bayes rule we will get Eqn2.9

$$p(x/y) = \frac{p(y/x)p(x)}{p(y)} \tag{2.9}$$

Here, $p(x/y)$ is the posterior probability, $p(x)$ is the prior probability and $p(y)$ is often taken as normalizing constant which can be ignored. According to maximum likelihood estimation, problem of maximizing $p(x/y)$ can be reduce to maximizing $p(y/x)$. Likelihood function p(y/x) follows Poission's distribution [38] and is given as

$$p(y/x) = \sum\nolimits_i (y_i ln(\sum\nolimits_j C_{ij}x_j) - \sum\nolimits_j C_{ij}x_j) \tag{2.10}$$

Here C_{ij} represents the sensitivity of detector i for activity in location j or in other words probability of photon generated at a point j being detected by detector at a point i. The above problem an ill posed and ill conditioned problem [30] [11] [38]. Moreover there is no closed form solution for estimation of x, which necessitates an iterative algorithm. An iterative method with guranteed convergance and give a closed form solution to the above equation is Maximum Likelihood Expectation Maximization [38].

$$x_j^{new} = \frac{x_j^{old}}{\sum_i C_{ij}} \sum_i C_{ij} \frac{y_i}{\sum_j C_{ij} x_j^{old}} \tag{2.11}$$

In Eqn.2.11 the comparison is made between estimated x_j^{old} and measured projection for each iteration. Thus the computation cost for every iteration is equivalent to that of FBP. There are basically three main drawbacks of Maximum Likelihood Expectation Maximization (MLEM) :

a) It converges to a noisy image

b) Slow convergence rate

c) Computationally expensive

To suppress noise, smoothing filters are usually applied to the reconstructed image and iterations are interrupted before convergence. A way to overcome the problem of slow convergence and to reduce the image noise is to replace the log likelihood criterion by a penalized likelihood function [30]. There are varieties of algorithms which are based on this concept [13], [14], [15], [34], [28]. An alternative to penalized likelihood method is another popular algorithm which is OSEM: Ordered Subset Expectation Maximization(OSEM)[20],[6]. OSEM is used to decrease to computational cost and accelerate the convergence. This method is based on ML-EM, the only difference is that in each iteration only small number of projections are being taken. Term 21 subset 2 iteration means that projection data was divided into 21 parts and each part is iterated twice, so total number of iterations equals $21 \times 2 = 42$.

FBP and iterative reconstruction methods are two common methods used for generating images from acquired sinogram for CT and PET respectively. In case of PET, strength of acquired signal (which is used for generating sinogram) is very weak which results in noisy and low resolution reconstructed images. Improving quality of such images is a major concern in medical imaging domain. In CT, though resolution of images is better than PET but work is going on to improve the quality further. After introdution of GPU and parallel programming, research is going on to use iterative reconstruction methods in CT. In our work we have maily focused on FBP based reconstruction.

Chapter 3

Motivation and Related work

Preserving details of upsampled reconstructed images is vital from clinical and detection perspective. The low resolution of PET images impede detection of finer details such as small tumors[40],[36]. Additionally when fusing PET with MRI images (which are twice as big), the challenge is to match the MRI image size prior to registration [32]. Synthetic zooming or upsampling deteriorates the quality of tomographic images.

With the given hardware image resolution can be improved in two ways : a) at data acquisition level, like increasing number of detectors, which is not practically feasible.
and b) by improving reconstruction algorithms or workflow.

Several methods or algorithms exist in literature which deal with improving quality or resolution of reconstructed images. Few have been discussed in previous section like ML-EM, OSEM, FBP etc. Researchers have also worked on improving volumetric image resolution. High resolution CT (HRCT) is another method to improve the resolution of lung (volumetric) images [2]. Here, the slice width and field of view(FOV) is reduced during the scanning in order to decrease the size of voxel. For PET, Dahlbom [9] [10] has shown that the axial resolution can be improved by aquiring sinogram data by shifting scanner table in discrete step while sampling the data appropriately. For CT Chen[7]and Besson[5] have come with specialized algorithms to imrpove the resolution during CT reconstruction. Chen algorithm is based on iterative reconstuction, where the reconstructed image is reprojected and combined with originally acquired projection data. It is then backprojected again at the higher resolution grid. Bessen's method increases the image resolution by increasing the number of samples in projection domain. Ideally, parallel projection data (sinogram) is generated by rebinning the fan projection (acquired data by scanner). In this approach, number of samples are increased during rebinning process via interpolation.

3.1 Image reconstruction on hexagonal lattice

The conventional type of lattice used to define an image is the square lattice. Many existing facts and studies motivated us to explore the possibility of using the hexagonal lattice for generating an upsampled reconstructed image. Mersereau [33] has shown that a regular hexagonal scheme is optimum for sampling circularly band limited two dimensional signals with least number of required sampling points. Hexagonal sampling requires less number of samples to represent the same information, consequently reducing the storage data space by 13.4% [26]. The hexagonal lattice also offers superior packing efficiency, uniform connectivity, additional equi-distant neighbors and 6-fold rotational symmetry [26]. Figure 3.1 shows that every point in the hex lattice is surrounded by six equidistant points, unlike square lattice where the ambiguity of four and eight fold neighborhood pertains. These factors have been shown to lead to better representation for curves among other benefits [37]. Figure. 3.2 shows the rotational symmetry of square and hexagonal sampling. Due to additional rotational symmetry an image sampled on a hexagonal lattice suffers less interpolation error under rotation as compared to image defined on a square lattice.

Reconstruction algorithms implemented using hexagonal lattice have been shown to give

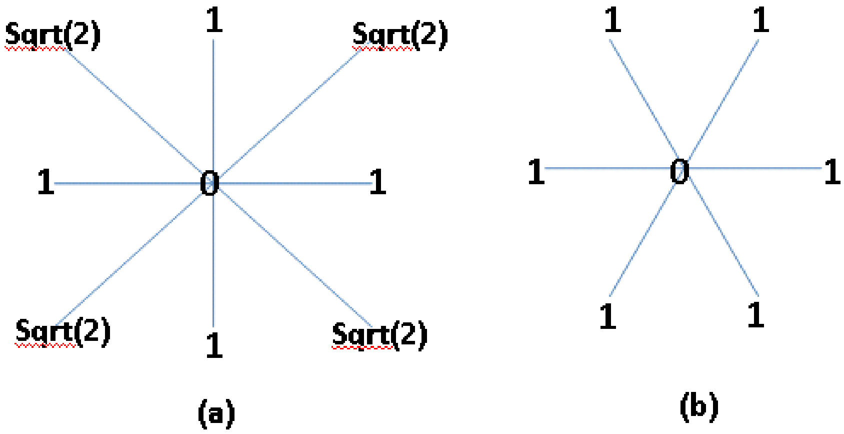

Figure 3.1: Distance map depicting nearest neighbor distance for (a) square and (b) hexagonal lattice

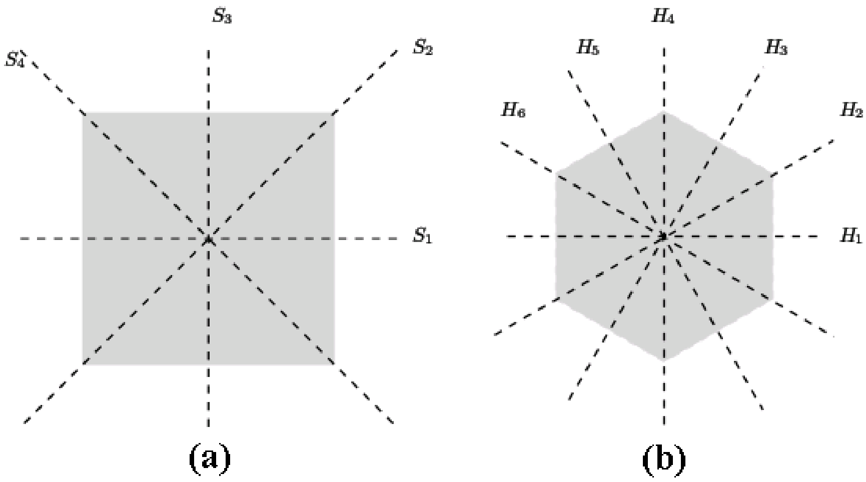

Figure 3.2: Rotational symmetry of (a)square (S1-S4) and (b) hexagonal (H1-H6) lattice

images with enhanced quality [3] and to incur reduced computational cost [27], since hexagonal lattice requires 13 percent less samples than square lattice to represent an image, which matters a lot in the reconstruction world. More recently, Faille et al.[16] have used hexagonal grid to reconstruct image from very sparse set of non-uniform samples via linear spline-based interpolation. This method generates good quality image in spite of the sparsity of the samples.

Hexagonal lattice has been studied and used as an alternative to conventional square lattice for reconstructing the images in tomogprahic world. In this thesis we will also explore the use of hex lattice to address the problem of high resolution image reconstruction.

3.2 Super resolution

In general, the concept of super resolution relies on using a combination of low resolution images which provide a *different view* of an object/scene. Translation and rotation are the possible ways in which these *different views* can be obtained. This technique is widely used in image processing [21] [4] [39]. For fan-beam CT, Izen et al. [35] have shown that the low resolution shifted images can be generated by standard fan-beam lattice and its reflected lattice. The union of these lattices have been used to increase the resolution by a factor of two. Kennedy et al. [25] utilised the concept of super resolution (SR) to generate PET images by acquiring multiple low resolution images sequentially, after translating or rotating the same object (or detector array) by a sub pixel distance with respect to the previous acquisition. Though this demonstrated the SR concept clearly, it was by directly applying the shifts and rotations to an object. In the case of a real patient, this is practically not feasible as it will increase the scan duration and it can also potentially increase the probability of patient movement during the scan.

Hence, an alternative was proposed by Chang [18] where the sub-pixel shifts were achieved in the reconstruction space. Specifically it was shown that it is possible to generate the desired low resolution images by introducing shifts in the reconstruction grids using the same sinogram data. A high resolution image is then generated by combining these low resolution images using an iterative super resolution algorithm. The approach that reconstructs 2-D signals from union of shifted lattices was originally proposed by Behmard [19]. Ideally to generate high resolution image with an upsampling factor of k, k^2 low resolution images are required to minimize artifacts. For example for upsampling factor of $k = 4$, 16 shifted low resolution images are combined with origin at $(0.25m, 0.25n)$; where $m = 0, ...5, n = 0.....5$. When k increases, method becomes computationally expensive. An improvement on this was investigated in [17], where a reduction in the required number of low resolution images was achieved with no degradation in the quality of the final image. Two new algorithms, namely ISR-1 (incomplete super resolution) and ISR-2 were presented which require only $2k - 1$ and k low resolution images respectively. For example, for $k = 4$ ISR-1 requires 7 low resolution images with sub-pixel shifts in the vertical and horixontal directions and ISR-2 requires only 4 low resolution images with shifts in diagonol direction Figure. 3.3. Visually, images generated by SR and ISR algorithms are of comparable quality.

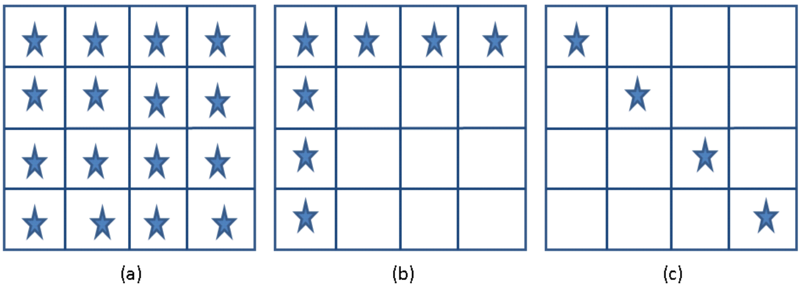

Figure 3.3: Required subpixel shifted low resolution images (marked by stars) required for deriving an up-sampled (by 4) image : (a) 16 with SR algorithm, (b) 7 with ISR-1 algorithm and (c) 4 with ISR-2 algorithm.

In this thesis, instead of translation we explored rotation as an alternative to generate super resolution images. High resolution image is generated by combining low resolution images which are rotated version of each other.

Chapter 4

Framework

In this chapter, we present two approaches for generating high quality up-sampled images. The techniques are based on samples drawn from:

(a)*A single lattice* : In this approach, we use samples defined on single hexagonal lattice for generating upsampled images.

(b)*Multiple lattice* :Here, an up-sampled image is generated using a super resolution technique by combining low resolution images which are defined on two rotated lattices.

4.1 Reconstruction on Hexagonal lattice

Our basic aim is to study the quality of upsampled (zoomed) reconstructed images when unconventional lattices are used instead of the square lattice. As discussed earlier its an established fact that hexagonal lattice can represent any circular band limited signal in a more efficient way than conventional square lattice. Moreover, it requires 13.4 percent less samples thus significantly reducing the computational costs. The two limitations of using hexagonal lattice are a) lack of hardware support and b) non orthogonal dependent axis. Unlike square lattice, the basis vectors of the hexagonal lattice subtend an angle of 60°. We propose to reconstruct using the hex lattice. In order to do this, we revisit the Radon

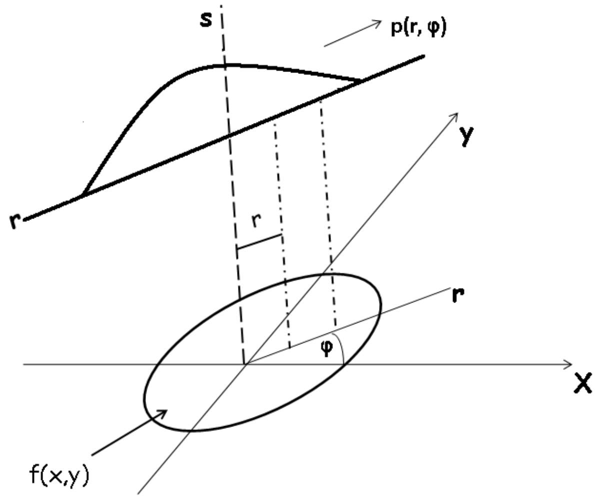

Figure 4.1: f(x,y) represents a function defined on hexagonal coordinate (x,y) and $p(r, \phi)$ is 1-D sinogram of f(x,y) defined over rotated (r,s) co-ordinate system

transform.

4.1.1 Radon transform with non-orthogonal basis

The non-orthogonal basis of interest is the set $[1, 0]^T, [\frac{\sqrt{3}}{2}, \frac{1}{2}]^T$ which underlies the hex lattice. The angle between these vectors is 60°.

The Radon transform for the new basis is given as(derived by us)

$$p(r, \phi) = R(f(x, y)) = \int_{-\infty}^{+\infty}\int_{-\infty}^{+\infty} f(x, y)\delta((\frac{1}{\text{sin60}}(x\text{sin}(60 + \phi) + y\text{sin}\phi) - r)dxdy \quad (4.1)$$

Here, the Radon transform $p(r, \phi)$ at an angle ϕ is defined as the integral of function f(x,y) for all x and y which satisfy the equation $(\frac{1}{\text{sin60}}(x\text{sin}(60 + \phi) + y\text{sin}\phi - r)) = 0$. The

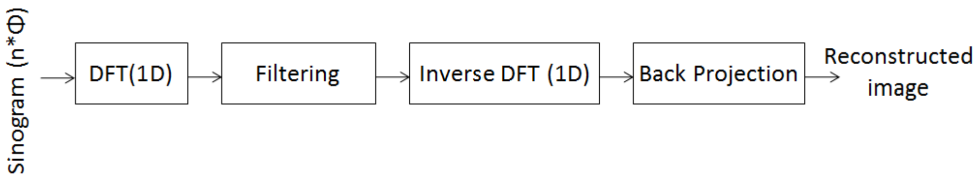

Figure 4.2: Filtered backprojection pipeline

coordinates (r, s) are related to (x, y) by a rotational matrix

$$\begin{bmatrix} r \\ s \end{bmatrix} = \frac{1}{\sin 60} \begin{bmatrix} \sin(60+\phi) & \sin\phi \\ -\sin\phi & \sin(60-\phi) \end{bmatrix} \begin{bmatrix} x \\ y \end{bmatrix} \tag{4.2}$$

$$\begin{bmatrix} x \\ y \end{bmatrix} = \frac{1}{\sin 60} \begin{bmatrix} \sin(60-\phi) & -\sin\phi \\ \sin\phi & \sin(60+\phi) \end{bmatrix} \begin{bmatrix} r \\ s \end{bmatrix} \tag{4.3}$$

Since (x, y) and (r, s) are related by a rotation transformation (refer to appendixB for detailed derivation), we can re-write eqn. 4.1 as

$$p(r,\phi) = R(f(x,y)) = \int_{-\infty}^{+\infty} f(\frac{1}{\sin 60}(r\sin(60-\phi) - s\sin\phi, r\sin\phi + s\sin(60+\phi)))ds \tag{4.4}$$

Eqn 4.4 can be generalized for any co-ordinate system with basis subtending an angle θ, as follows

$$p(r,\phi) = R(f(x,y)) = \int_{-\infty}^{+\infty} f(\frac{1}{\sin\theta}(r\sin(\theta-\phi) - s\sin\phi, r\sin\phi + s\sin(\theta+\phi)))ds \tag{4.5}$$

Sampling this projection function produces the discrete sinogram $p(r_i; \phi_j)$.

4.1.2 Method

In this section, we present our approach for generating an upsampled image from data defined on a hexagonal lattice, where $\theta = 60°$.

Let I(x, y) be the imaged object and $p(r, \phi)$ be the corresponding sinogram data where (r, ϕ) are both discrete. The process of reconstruction as described by Chang et al.[18] consists

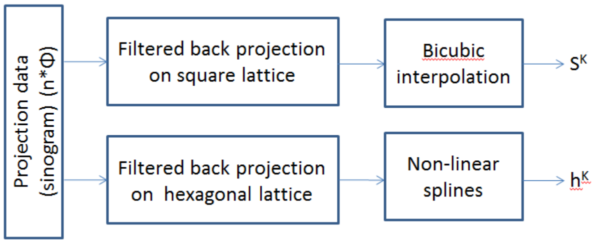

Figure 4.3: Up-sampling (by k) pipeline

of two main steps: back-projection of $p(r, \phi)$ into a continuous image $I_c(x, y)$ and sampling it to generate a digital image $I_D[n1, n2]$ where [n1, n2] are discrete. Algorithm used for implementing Filtered backprojection (FBP) is the same as discussed in chapter 2 and is explained in Figure 4.2. The back projection is done onto a hexagonal lattice. The desired upsampled image is generated from samples defined on hex lattice via interpolation.

4.1.3 Algorithm and implementation details

For validation and comparison we also generated an upsampled image from a low resolution image reconstructed onto a square lattice as well.

a) The sinogram is backprojected onto two different lattices Square (S) and Hexagonal (H) via different backprojector (BP) operator BP_{sq} and BP_{hex} respectively using the Filtered Back Projection (FBP) algorithm described in Figure 4.2.

b) Upsampled images are generated from the square and hexagonal lattice using bicubic interpolation kernel and non-linear splines respectively. Figure 4.3 shows the process pipeline. For display purposes, the upsampled image was resampled onto a square lattice.

4.2 Super resolution

Super resolution has been explored as a second method to improve the quality of upsampled reconstructed images. A high resolution image is generated by combining 2 or more low resolution images. Low resolution images can be generated by translation or rotation. Although both were demonstrated in [25] by directly manipulating a phantom, the methods in [18] and [17] have only focused on translation by sub-pixel shifts. We examined generating upsampled tomographic images by combining samples from *two* low resolution images which are rotated versions of each other. These low resolution images are defined on square or hexagonal lattice and are derived from the same sinogram data, as in [18]. Samples from these lattices are interpolated to generate an up-sampled image defined on a square lattice.

Combination of samples from the rotated lattices for both square and hexagonal sampling is shown Figure 4.4. An interesting point that can be observed is that the union operation on the two rotated lattices breaks up the periodicity and hence the result is in a non-uniformly sampled space. However, there is some quasi-periodicity in this space. This is in contrast to the samples in union of shifted lattices, where they always lie in a periodic lattice.

Let $p(r, \phi)$, $p(r, \phi + \delta\phi)$ be sinograms acquired for the object without and with rotation respectively. Images generated from these (by applying back projection operator BP) can be represented in polar coordinates as $I_0(r, \phi)$ and $I(r, \phi + \delta\phi)$ respectively. Mathematically it can be written as:

$$BP(p(r, \phi)) = I_0(r, \phi) + n_0(r, \phi) \tag{4.6}$$

$$BP(p(r, \phi + \delta\phi)) = I(r, \phi + \delta\phi) + n_1(r, \phi) \tag{4.7}$$

The noise terms $n_0(r, \phi)$ and $n_1(r, \phi + \delta\phi)$ in the above equations differ because of different acquisition.

Now let us consider generating low resolution images by back projecting the sinogram

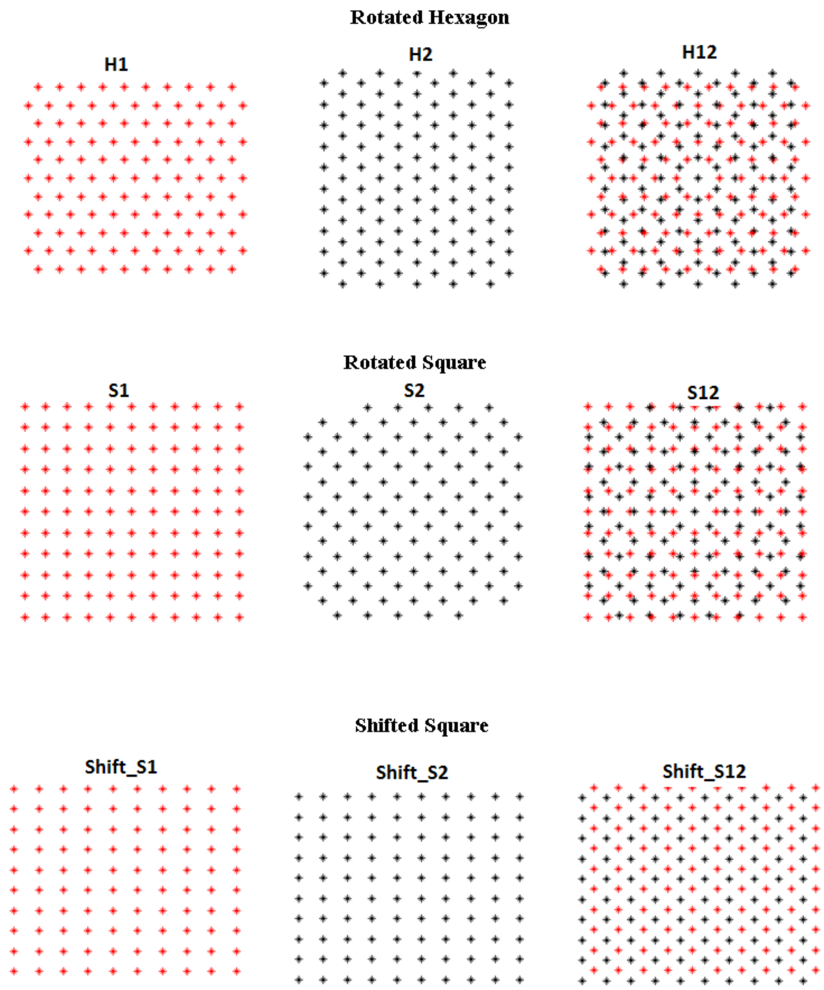

Figure 4.4: Row 1 Rotated Hexagon : $H1$ shows samples on hex lattice with basis vector $(1/2, 1), (0, \sqrt{3}/2)$. $H2$ shows the samples on rotated hex lattice generated by rotating H1 basis vectors by 30 . $H12$ (union of rotated lattice) shows quasi-periodic sampled samples generated by combining $H1$ and $H2$. Row 2 Rotated square: $S1$ shows samples on square lattice with basis vector $(1, 0), (0, 1)$. $S2$ shows the samples on rotated square lattice generated by rotating S1 basis vectors by 45. $S12$ (union of rotated lattice) shows quasi-periodic sampled samples generated by combining $S1$ and $S2$. Row 3 Shifted Square: $Shift\_S1$ shows samples on square lattice with centre at (0,0). $Shift\_S2$ shows the samples on shifted square lattice with centre at $(1/2, 1/2)$. $Shift\_S12$ (union of shifted lattice) shows periodic sampled samples generated by combining $Shift\_S1$ and $Shift\_S2$.

$p(r, \phi)$ onto rotated lattices. The result of back projection will be,

$$BP_{\delta\phi}(p(r, \phi)) = I(r, \phi + \delta\phi) + n_0(r, \phi + \delta\phi) \tag{4.8}$$

Here, $BP_{\delta\phi}$ is a BP operator that generates an image onto a lattice rotated by an angle $\delta\phi$. When $\delta\phi = 0$ we get the image on the canonical lattice as in eqn.4.6. If we apply $BP_{\delta\phi}$ on sinogram $p(r, \phi)$ we will get an image similar to eqn.4.7 and added noise content $n_0(r, \phi + \delta\phi)$ which is rotated version of noise described in eqn.4.6.

In the Fourier domain we can clearly visualize the difference and similarity between the three equations. An image I(x,y) can be represented in polar coordinate as $I(r, \theta)$ and its Fourier transform $I(R, \Theta)$ is represented in terms of Bessel function J_n (refer to appendix for details) as :

$$\begin{align}
F(I_0(r, \phi)) &= I_0(R, \Theta) \tag{4.9}\\
&= \sum_{-\infty}^{n=+\infty} \int_0^{+\infty} [\int_0^{2\pi} I(r, \phi) e^{in\phi} d\phi] i^n J_n(2\pi r R) e^{-in\Theta} r dr \tag{4.10}\\
&= \sum_{-\infty}^{n=+\infty} i^n I_n \tag{4.11}
\end{align}$$

$$I_n = \int_0^{+\infty} [\int_0^{2\pi} I(r, \phi) e^{in\phi} d\phi] J_n(2\pi r R) e^{-in\Theta} r dr \tag{4.12}$$

The Fourier transform of a rotated (by an angle $\delta\phi$) image,

$$\begin{align}
F(I_0(r, \phi + \delta\phi)) &= I_0(R, \Theta + \delta\phi) \tag{4.13}\\
&= \sum_{-\infty}^{n=+\infty} \int_0^{+\infty} [\int_0^{2\pi} I(r, \phi) e^{in\phi} d\phi] J_n(2\pi r R) e^{-in(\Theta + \delta\phi)} r dr \tag{4.14}\\
&= \sum_{-\infty}^{+\infty} i^n I_n e^{-in\delta\phi} \tag{4.15}
\end{align}$$

Computing Fourier transform of eqns 4.6, 4.7, 4.8 using the above equations, we have

$$F(BP(p(r,\phi))) = \sum_{n=-\infty}^{+\infty} i^n I_n + \sum_{n=-\infty}^{+\infty} i^n N_{n0} \tag{4.16}$$

$$F(BP(p(r,\phi+\delta\phi))) = \sum_{n=-\infty}^{+\infty} i^n I_n e^{-in\delta\phi} + \sum_{n=-\infty}^{+\infty} i^n N_{n1} \tag{4.17}$$

$$F(BP_{\delta\phi}(p(r,\phi))) = \sum_{n=-\infty}^{+\infty} i^n I_n e^{-in\delta\phi} + \sum_{n=-\infty}^{+\infty} i^n N_{n0} e^{-in\delta\phi} \tag{4.18}$$

From Eqns 4.15, 4.16 and 4.17 its quite evident that low resolution images generated by rotating the object contain different noise content because of different acquisition. Where as, the images generated by backprojecting the sinogram on rotated latticed contain similar noise content which differs in phase when represented in polar coordinate. The phase difference in low resolution images indicate that the combination will supress imaging, but still more theoretical exploration is needed to understand the entire mechanism (refer appendix for detailed derivation). In the above equations, n is the periodicity which depends on number of angular samples in reconstruction domain. For example if we have a sinogram of size $(151 * 180)$ where 151 is the number of radial samples and 180 is the number of angular samples, then the periodicity n equals 180.

4.2.1 Method and implementation details

In this section, we present our approach for generating high resolution image via union of two low resolution images defined on rotated lattices. We refer to this as URL.

Step 1: Reconstructing Low resolution Images

We know that the sinogram data contains continuous information about the object. Hence, it can be backprojected onto more than one lattice with subpixel shifts. We generate these desired sets by sampling continuous image $I_c(x, y)$ with two lattices which are rotated versions of each other. Consider 2×2 sampling matrices V and $V_\phi = A_\phi V$ where A_ϕ is a rotation matrix. The desired sets of samples I_R and I_{R_ϕ} are then given as:

$$I_R[n] = I_c(Vn) \tag{4.19}$$

$$I_{R_\phi}[n] = I_c(V_\phi n) \tag{4.20}$$

where $n = [n1, n2]^T$. The sampling matrix V will vary with the choice of the underlying lattice, either square or hexagonal. Hexagonal lattices offer superior packing efficiency with non-orthogonal bases [3], [27] and hence have been considered. Sampling matrices for square and hexagon are given as follows:

$$V_{sq} = \begin{bmatrix} \cos\phi & \sin\phi \\ -\sin\phi & \cos\phi \end{bmatrix} \tag{4.21}$$

$$V_{hex} = \frac{1}{\sin 60} \begin{bmatrix} \sin(60+\phi) & \sin\phi \\ -\sin\phi & \sin(60-\phi) \end{bmatrix} \tag{4.22}$$

Step2: Generating Upsampled Images

Given a sinogram data $p(r, \phi)$, we first reconstruct two images, namely I_R and I_{R_ϕ} using FBP and Equations 4.6 and 4.8. Next, we derive an upsampled (by k) image denoted as URL^k by interpolating between the samples of I_R and I_{R_ϕ} as follows:

$$URL_k = (I_R + I_{R_\phi}) * h \tag{4.23}$$

where * denotes convolution and h is an interpolating function. Since two different lattices were considered in our work, the results obtained with the square and hexagonal lattices are denoted as URL^k_{sq} and URL^k_{hex} respectively. The complete pipeline of processing for generating upsampled image is shown in Figure .4.5.

Implementation details: Since combination of rotated lattices generates quasi-periodic samples, thin plate splines were chosen to interpolate between them and to generate the desired samples on an upsampled lattice. The computed samples were always defined to be on

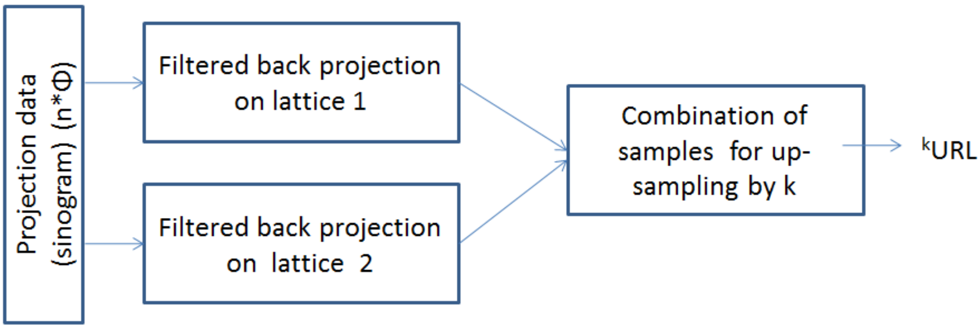

Figure 4.5: Pipeline for generating URL images, lattice 2 is a rotated version of lattice 1

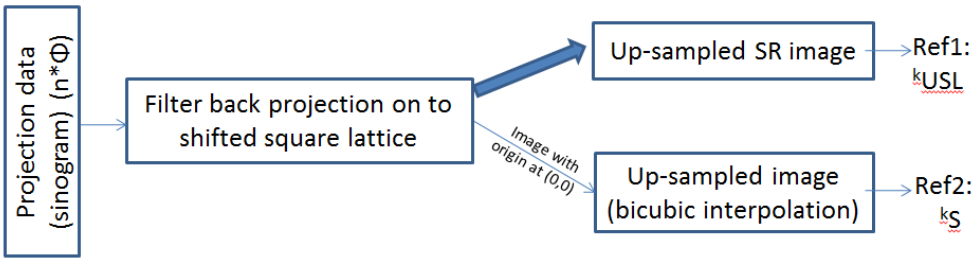

Figure 4.6: Generating reference images for validation of results

a square lattice regardless of the original (low resolution) lattices for display on conventional devices. The angle of rotation ϕ was taken to be 45 and 30 degree for square and hexagonal lattices, respectively, to minimize overlap between I_R and I_{R_ϕ} sample points. Hexagonal lattices with basis vectors $(1, 0), (1/\sqrt{3}, 1)$ and $(1, 1/\sqrt{3}, (0, 1)$ were used to generate a good distribution of samples. Up-sampling factors of k = 2, 4 and 6 were considered in our experiments.

Step3: Assessment of proposed method

A second pipeline shown in Figure. 4.6 was constructed to validate the results of the proposed method. Here two up-sampled images were generated using direct up-sampling of the reconstructed image I_R and super resolution algorithm ISR-2 [17].

a) **Direct upsampled images**$S^k(ref1)$: The input sinogram was filtered and back projected onto a square lattice using the FBP algorithm. This was next up-sampled using bi-cubic interpolation to obtain image S^k.

b) **Union of shifted lattices** USL^k $(ref2)$: The FBP algorithm was used to generate sub-pixel shifted images defined on square lattices. The number of such generated images depends on the up-sampling factor k and the super resolution (SR) algorithm. For example, to up-sample by a factor of 4 via a basic SR method (based on union of shifted lattices), 16 images are required. However, ISR1 and ISR2 algorithms described in [17] require only 7 and 4 images respectively. These images are used to generate up-sampled image USL^k via SR technique.

Implementation details: Ideally for an upsampling factor of k, k^2 subpixel shifted images are needed to generate high resolution image. It has been shown in [17] that high resolution images of similar quality can be obtained by combining just k subpixel diagonal shifted images. Hence, diagonal shifted low resolution images were reconstructed with the FBP algorithm. Samples from these images were interpolated using a bicubic kernel to generate desired samples on a high resolution grid (upsampled image). Subpixel shifted images were generated using Fesslers toolbox [12] and combined via Vandewalles toolbox [31] using existing interpolation algorithms.

Chapter 5

Phantom and Quality Metric

In this chapter, we present the discussion about the phantom and quality metrics used in our study.

5.1 Phantoms

Phantoms are specially designed objects that are scanned or imaged to evaluate, analyze, and tune the performance of various imaging devices. Phantoms often have properties similar to human tissue. Three analytical phantoms namely *concentric rings,lines* and *dots* and two PET phantoms: $NEMA$ and $HOFFMAN$ brain phantom were used to study the effects of upsampling samples from union of rotated lattice. Analytical phantoms were generated using equation described in [22].

a) Concentric rings: concentric rings phantom Figure. 5.1 was generated to study the preservation of curved structure in the up sampled image and the effectiveness of an upsampling method in suppressing imaging. Images were reconstructed from sinogram of size 151×180.

b) Lines : Lines phantom Figure 5.2 was used to study the preservation of linear structures by different methods of upsampling. Images were reconstructed from sinogram of size

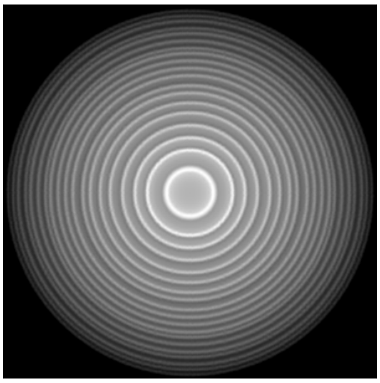

Figure 5.1: Concentric rings

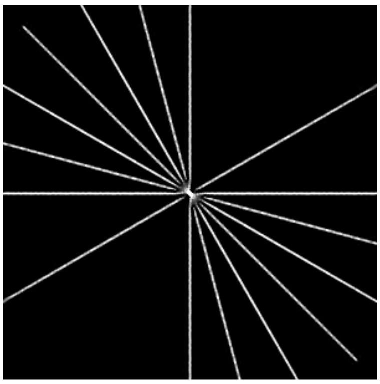

Figure 5.2: Lines

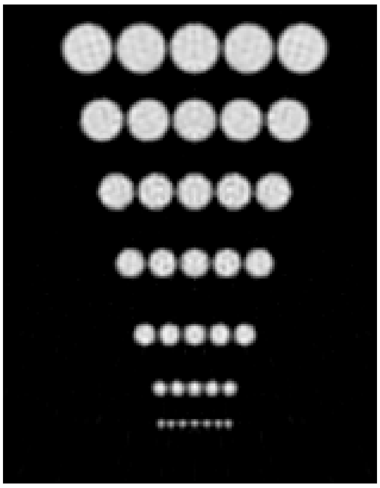

Figure 5.3: Dots

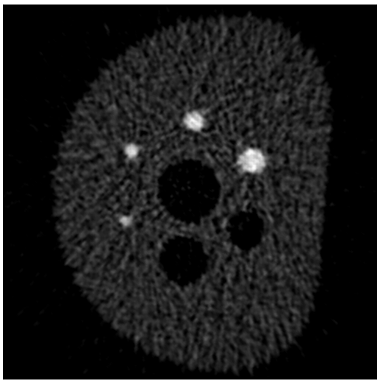

Figure 5.4: Nema Phantom

121x180.

c) Dots: The dots phantom Figure 5.3 was created to compare the contrast and spatial resolution of the up-sampled image using the line profile and contrast ratio. Images were reconstructed from sinogram of size 101x180.

d) NEMA phantom: NEMA(National Electronics Manufacturers Association) phantom Figure 5.4 is a standard PET phantom used in evalution of reconstructed image quality[1]. We used it to study the contrast of the upsampled image and the effectiveness of an upsampling method in supressing the imaging. NEMA sinogram is of size 293x280.

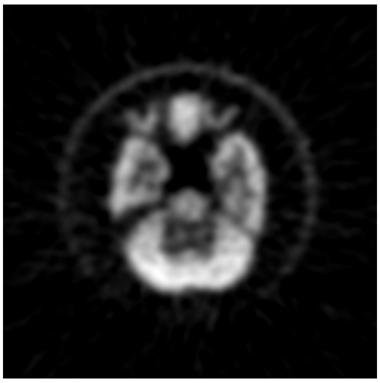

Figure 5.5: Hoffman brain phantom

e)Hoffman brain phantom: The Hoffman 3-D Brain Phantom Figure 5.5 provides the anatomically accurate three dimensional simulation of the radioisotope distribution found in the normal brain [1]. We used it mainly to study the effect of up-sampling on quality of image in terms if noise content and contrast. Hoffman brain phantom is a 3D phantom of size 367x315x91.

5.2 Quality Metric

We have used three quality metrics in our study. The metrics are explained below: a) Energy Distribution plots: Power spectrum can give a clear picture about the aliasing artifacts. We computed energy distribution plot in radial and angluar (wedge) directions from normalized power spectrum of an image using IQM toolbox [29]. Angular plot was generated by taking summation of blocks of normalized spectrum at an angle of 4 degrees and radial plot was generated by dividing the normalized spectrum into 64 rings and then summing them. Figure 5.6 show sample radial and wedge plots respectively.

b) Line plot: A quantitative evaluation of the contrast was carried out by taking the intensity profile of selected region of interest (ROI) of the image and using the contrast ratio

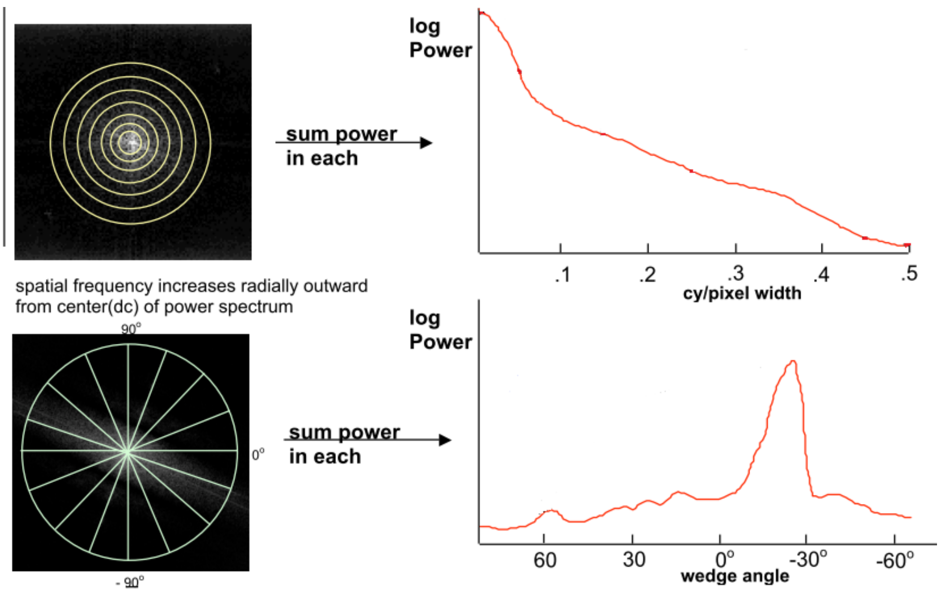

Figure 5.6: Energy distribution plots in radial and angular(wedge) directions (source [29])

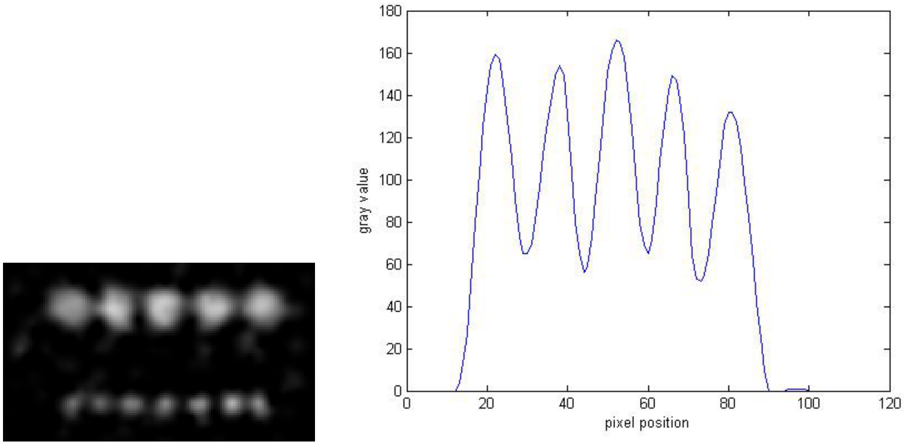

Figure 5.7: Line profiles of the 1st row for Dots.

[17] defined as follows.

$$CR = \frac{\frac{1}{m}\sum_{i=1}^{m} P_i - \frac{1}{n}\sum_{j=1}^{n} T_j}{\frac{1}{m}\sum_{i=1}^{m} P_i} \tag{5.1}$$

where m and n are number of peaks and troughs respectively, P_i is the amplitude of the ith peak and T_j is the amplitude value of the jth trough. For example, line profile of 1st line of the image shown in Figure 5.7 (a) has five dots and hence the line profile will have five peaks and six throughs, as shown by Figure 5.7(b).

c) Noise Spectra: We also studied the noise characteristics by computing the spectrum of a uniform ROI in the image which has no objects.

Chapter 6

Results and Discussion

We have two sets of images, a) high resolution image generated from samples defined on hexagonal grid H

b) high resolution image generated by combining two low resolution images defined on rotated lattice URL (union of rotated lattices).

For validation, we will compare H with direct upsampled image S and URL with image generated by combination of images defined on subpixel shifted lattice (USL: union of shifted lattice) and S. We compared all the images i.e *S,H,URL, USL* together for better understanding and readability.

6.1 Concentric Rings

As discussed earlier, the concentric rings phantom was used to study the preservation of curved structure in the up-sampled image and the effectiveness of an up-sampling method in suppressing imaging. Images were reconstructed from a sinogram of size 151×180 by implementing the FBP algorithm. Figure 6.1 (a), (b), (c), (d) and (e) show one quadrant of the up-sampled S^4, H^4, URL^4_{sq}, $URL^4_{hex}$and USL^4 images (up-sampling factor 4) of the

(a) S^4

(b) H^4

(c) URL^4_{sq}

(d) URL^4_{hex}

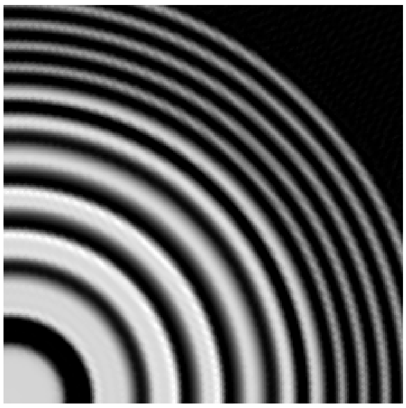

(e) USL^4

Figure 6.1: Upsampled results for Concentric rings (only 1 quadrant is shown)

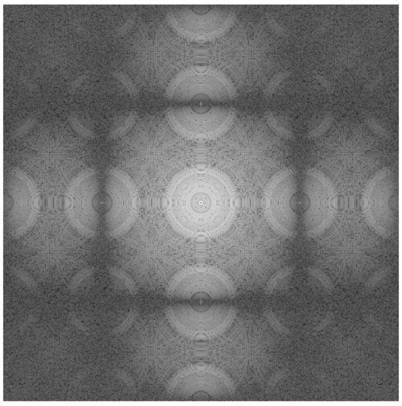

(a) S^4

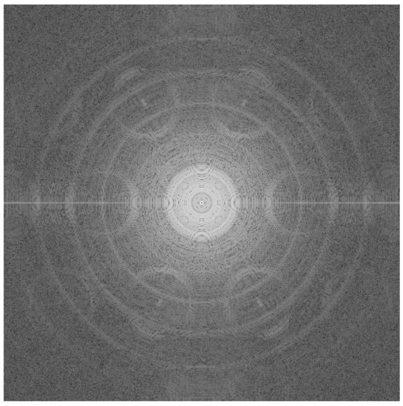

(b) H^4

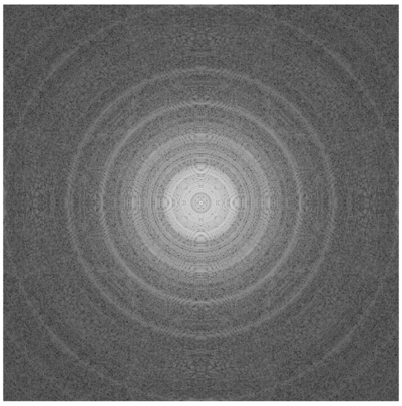

(c) URL^4_{sq}

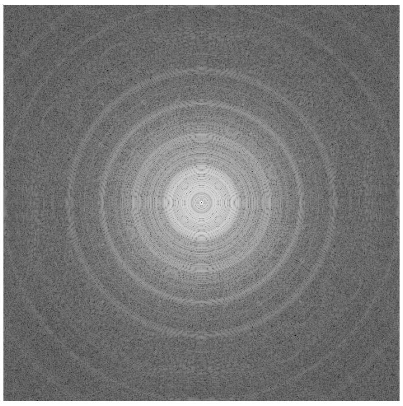

(d) URL^4_{hex}

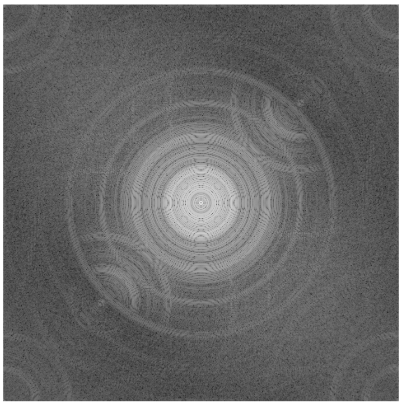

(e) USL^4

Figure 6.2: corresponding full amplitude spectra of upsampled concentric rings.

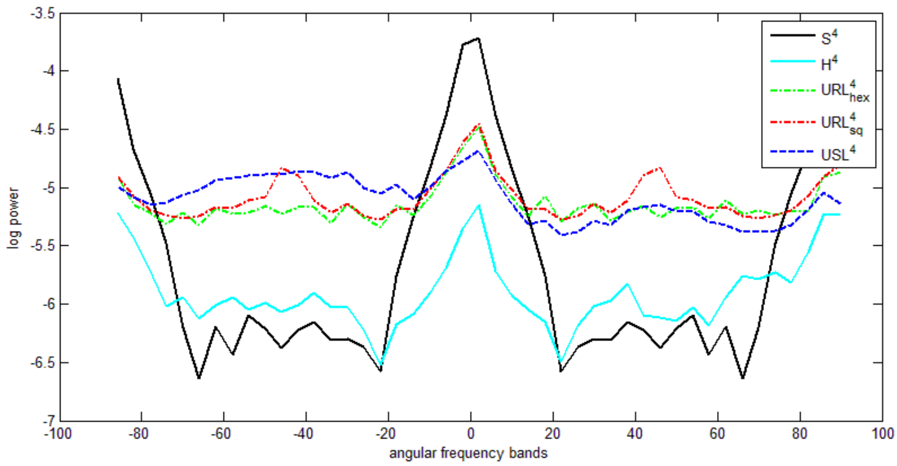

(a) Angular energy plot

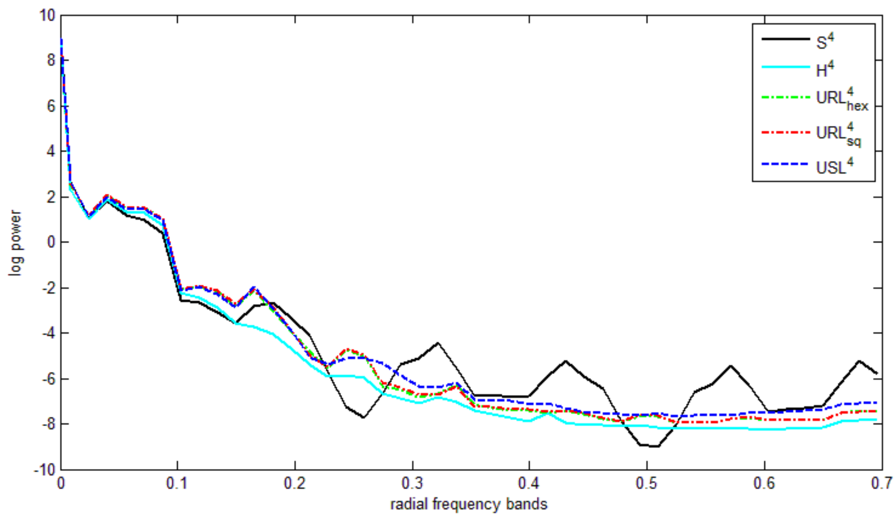

(b) Radial energy plot

Figure 6.3: Angular and radial energy plot of concentric rings for different upsampling methods

concentric rings phantom while Figure 6.2 (a), (b), (c), (d) and (e) show their corresponding amplitude spectra. While up-sampling an image, our aim is to preserve details and definition of the image but prevent imaging. In the Figure 6.1, it is visually evident that URL and USL images preserve the definition of curves. The S naive/direct upsampled result exhibits aliasing and distortion which is to be expected. From the spectra in Figure 6.1 we can clearly see that in H, image aliasing is present but is less compared to S. Visually also curved structures are well defined in H than S. The energy distribution computed from the normalized power spectrum of an image in angular direction is shown in Figure 6.3(a) and radial direction is shown in Figure 6.3(b). The energy variation across ρ is seen to be much smoother for H, USL and URL compared to S due to reduction in imaging. On an average, there is a boost in energy for all angles over URL_{hex} with a directional bias evident at 45 for URL_{sq}. USL images shows prominent increase of energy from $-90°$ to $0°$ compared to URL. This is because USL image was generated using ISR-1 algorithm, which combines diagonally shifted images for generating high quality upsampled image.

6.2 Lines

Lines phantom was used to study the preservation of linear structures by different methods of upsampling. Images are reconstructed from sinogram of size 121×180 using the FBP algorithm. The quality of the images were evaluated visually. Figure 6.4 (a), (b), (c), (d) and (e) show the up-sampled S^4,H^4,URL^4_{sq}, $URL^4_{hex}$and USL^4 images (up-sampling factor 4) of the lines at angles 0°, 15°, 30°, 45°, 60°, 75° and 90°. The lines are crisper and well defined in URL images compared to USL and S images. In USL image, the vertical line becomes blurred towards the periphery of the image and is not well defined in Figure 6.4(e) even though this grid supports a good representation for a line at this angle. In the S image, distortion is present in all the lines except the one in vertical direction. In the H image,

(a) S^4

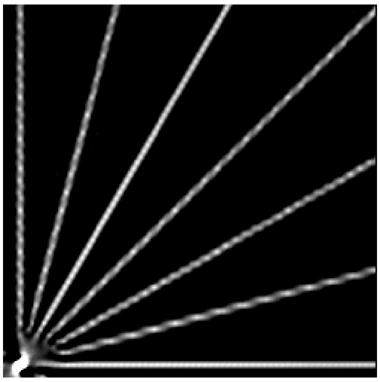

(b) S^4

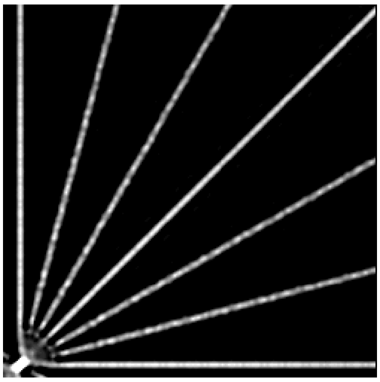

(c) URL^4_{sq}

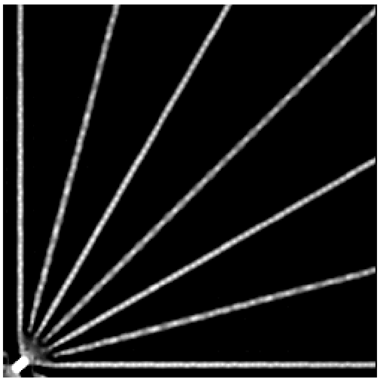

(d) URL^4_{hex}

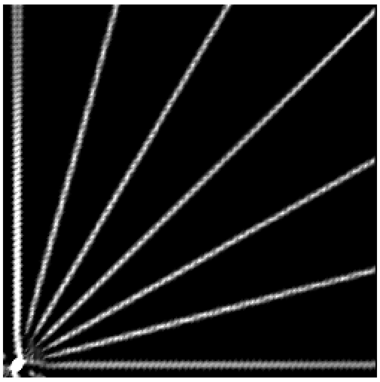

(e) USL^4

Figure 6.4: Upsampled results for Lines

distortion is present for all the lines except for one at an angle of 60°. Lines at an angle of 45° and 75° are also well defined in H as compare to S.

6.3 Dots

The dots phantom was used to compare the contrast and spatial resolution of the up-sampled image using line profiles and contrast ratio. Images were reconstructed from a noisy sinogram of size 101×180 by implementing FBP and OSEM. Figure 6.5 (a), (b), (c), (d) and (e) show the up-sampled S^4,URL^4_{sq}, $URL^4_{hex}$and USL^4 images reconstructed using FBP. OSEM has been implemented to improve the SNR of the reconstructed image. OSEM generated upsampled images are shown in Figure 6.7 (a) through (c). Figure 6.10 (a), (b) and (c) show the ROI of up-sampled S^6, URL^6_{sq} and USL^6 images reconstructed using OSEM.Visually, URL_sq appears noisier than URL_hex and USL. This is partially due to the fact that the latter two are of similar quality but with higher contrast.

A quantitative evaluation of the contrast was carried out by taking the intensity profile in the last 2 lines of the image and using the contrast ratio given in chapter 4. The obtained contrast values are tabulated in Table 6.1. From this table it is seen that OSEM helps increase the contrast of the reconstructed images by suppressing noise. Since upsampling by USL and URL method can introduce noise, we studied the spectra of a noisy ROI in these images. The 41×41 ROI and the obtained amplitude spectra (with dc suppression) are shown in Figure 6.9. The URL introduces less noise than USL as evident from the circularly symmetric pattern of the former spectra compared to the wider bandwidth of the spectra in the case of USL. Prominent distortion in line profile for penultimate row of dots also suggests that noise content in USL is more than URL.

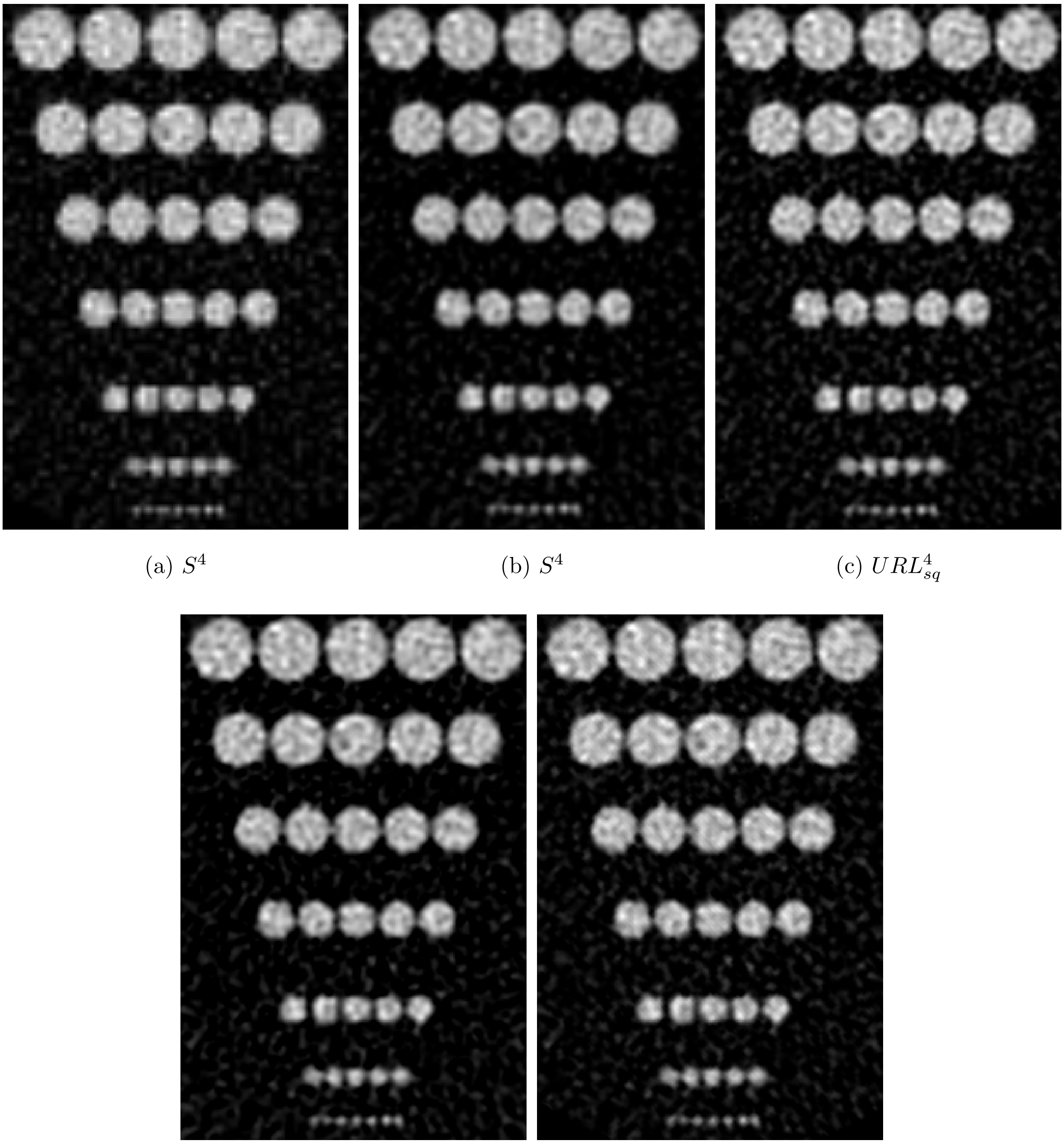

(a) S^4 (b) S^4 (c) URL^4_{sq}

(d) URL^4_{hex} (e) USL^4

Figure 6.5: FBP- based upsampled (k=4) results ((a) through (d))for Dots.

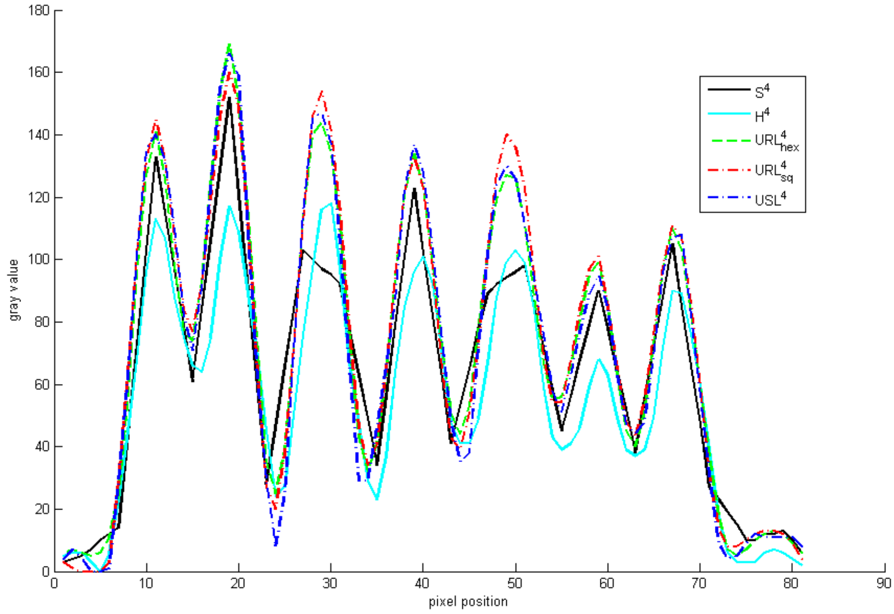

(a) Line profile of the last row

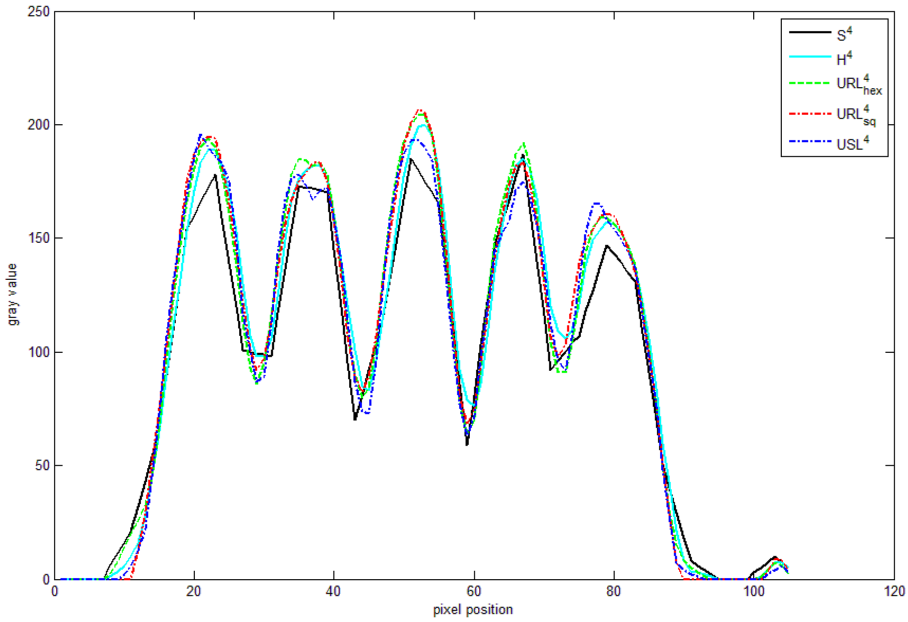

(b) Line profile of the penultimate row

Figure 6.6: FBP: Line profiles of the last two rows for Dots.

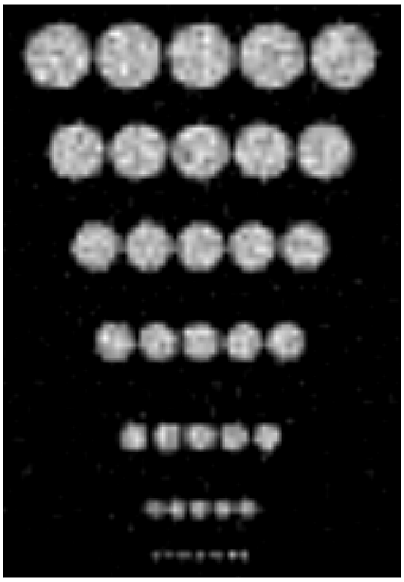

(a) S^4

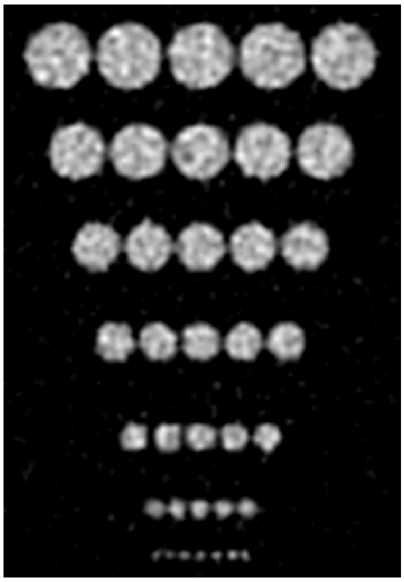

(b) URL_{sq}^4

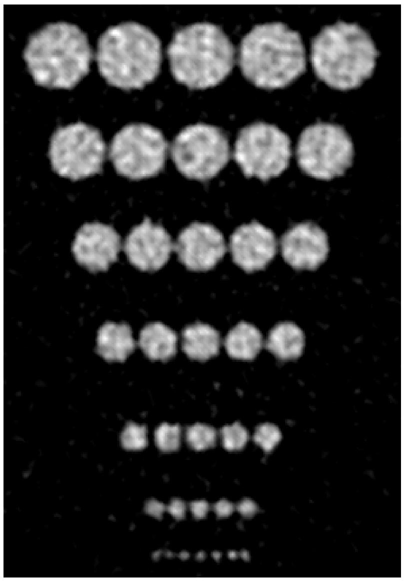

(c) USL^4

Figure 6.7: OSEM- based upsampled (k=4) results ((a) through (c)). for Dots

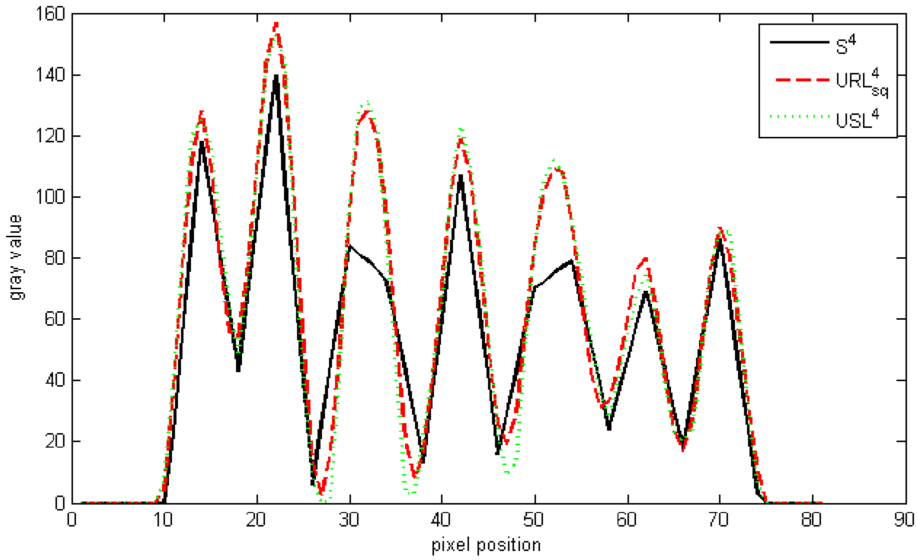

(a) Line profile of the last row

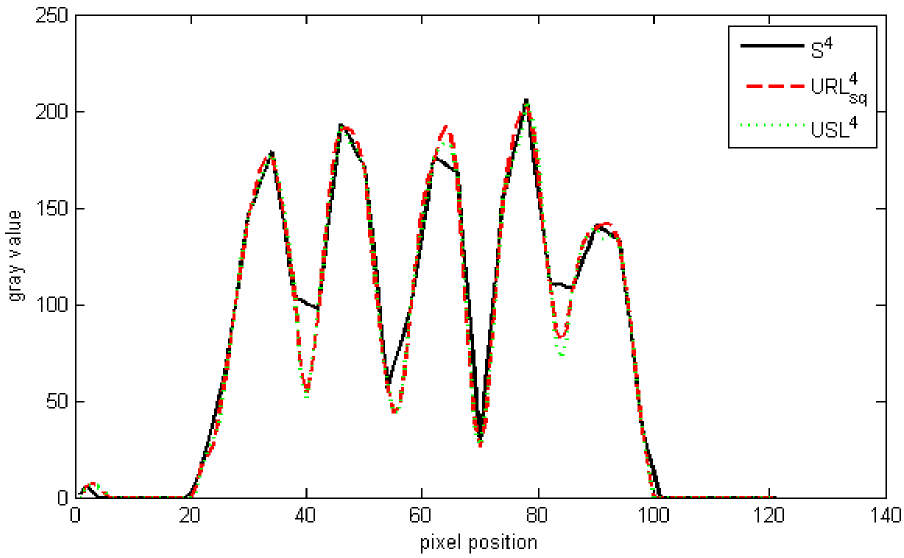

(b) Line profile of the penultimate row

Figure 6.8: OSEM- line profiles of the last two rows for Dots

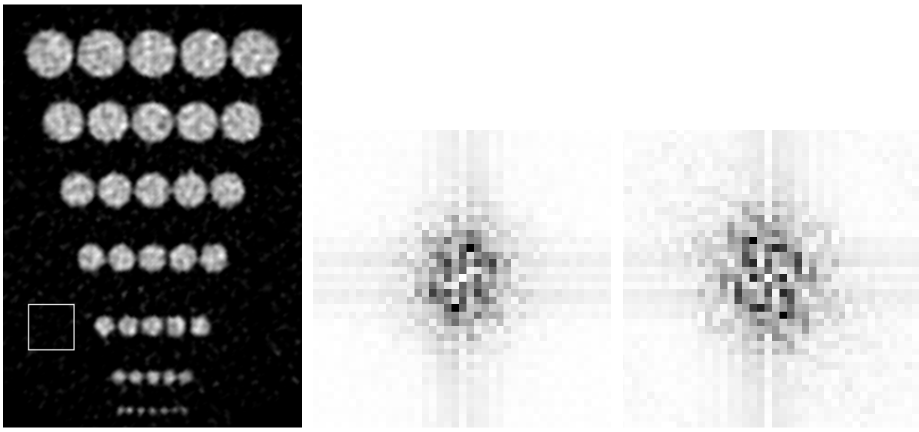

(a) ROI (b) URL_{sq}^4 (c) USL^4

Figure 6.9: A noisy ROI (shown by square) of Dots phantom and its noise spectra

Implementation details for OESM: The quality of tomographic images are adversely affected by the introduction of noise during the acquisition process. For PET/SPECT imaging, the strength of detected signal (projection or sinogram data) is very weak compared to CT and MR images which results in poor resolution (typically 128×128) and decrease in SNR (signal to noise ratio) of the reconstructed images. Traditional iterative methods like Maximum Likelihood-Expectation Maximization (ML-EM) or ordered subsets expectation maximization (OSEM) are used for improving the image quality. OSEM uses FBP generated image as an initial estimate, and improves the quality iteratively [12]. Reconstructed image for dot phantom was done using the OSEM reconstruction algorithm (21 subset, 2 iteration) implementation in the Fessler's toolbox.

In CT imaging there are two types of noise, 1) electrical noise or roundoff error which can be modeled as additive noise and 2) shot noise which can be modeled as Poisson distribution [24]. In the case of PET imaging, shot noise is prominent [23]. We assume sufficiently large mean for the Poisson noise and hence approximate it with a Gaussian distribution. Thus, for generating the sinogram data suitable for both the modalities, additive Gaussian noise (0 mean, standard deviation =0.001) was added to the analytical sinogram.

(a) S^6 (b) URL^6_{sq} (c) USL^6

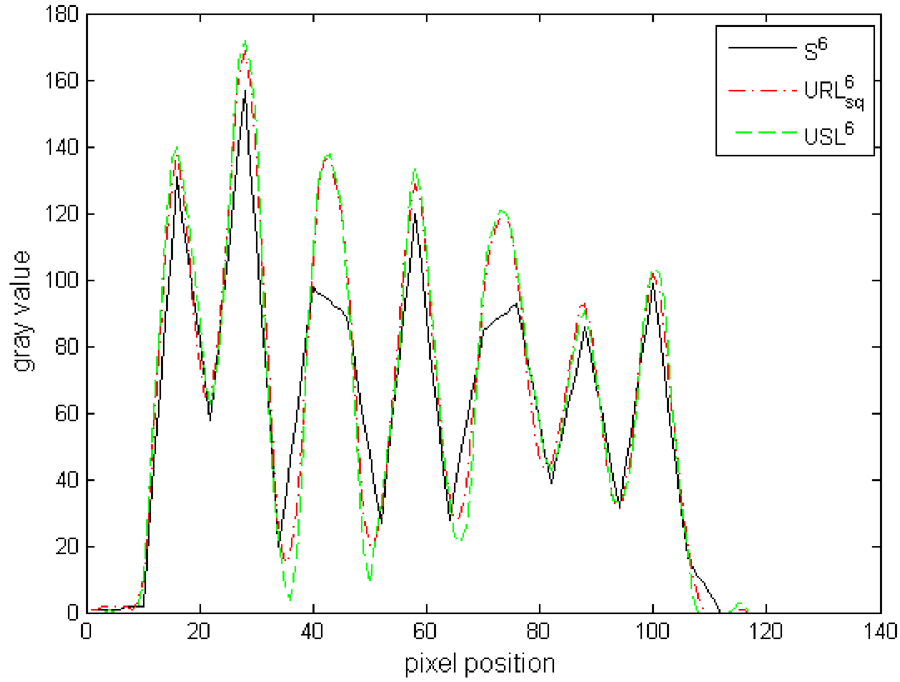

(d) Line profile of the last row

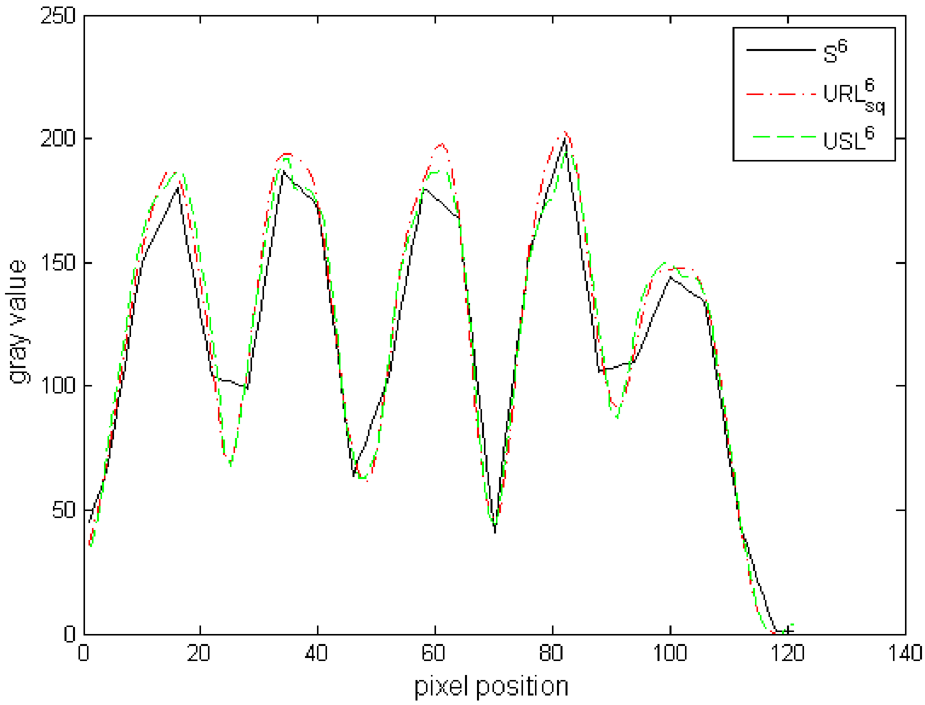

(e) Line profile of the penultimate row

Figure 6.10: OSEM-based upsampled (k=6) results for Dots displaying last two rows of dots and the corresponding line profiles

Table 6.1: Contrast ratio across last two lines of the Dots Phantom

Upsamp results	FBP		OSEM			
-	k=4		k=4		k=6	
-	second last row	last row	second last row	last row	second last row	last row
S^4	0.5406	0.6086	0.5801	0.7036	0.5752	0.6964
USL^4	0.5645	0.6516	0.6235	0.7730	0.6153	0.7861
URL^4_{sq}	0.5717	0.6638	0.6326	0.7441	0.6273	0.7527
URL^4_{hex}	0.5581	0.6534	-	-	-	-
H^4	0.5262	0.5874	-	-	-	-

6.4 NEMA Phantom

NEMA phantom was used to study the contrast of the up-sampled image and the effectiveness of an up-sampling method in suppressing imaging. Figure 6.11 (a), (b), (c), (d) and (e) show the up-sampled S^4,URL^4_{sq}, $URL^4_{hex}$and USL^4 images (up-sampling factor 4) of the NEMA phantom while Figure 6.12(a), (b), (c), (d) and (e) show their corresponding amplitude spectra. While up-sampling an image, our aim is to preserve details and definition of the image and prevent imaging. The energy distribution plot shown in Figure 6.14, illustrates a smooth variation for the image URL obtained by our proposed method. In contrast, the energy distribution of the images S^4 and USL^4 have prominent irregularities beyond the baseband, thus indicating presence of imaging. Figure 6.13 illustrate the intensity variation in the radial direction across the smallest circle (sphere) in the phantom.

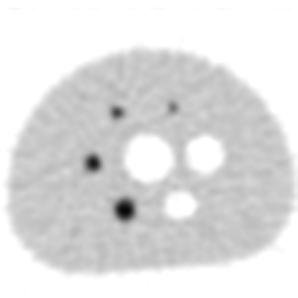

(a) S^4

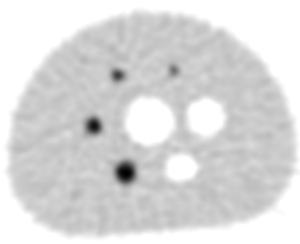

(b) H^4

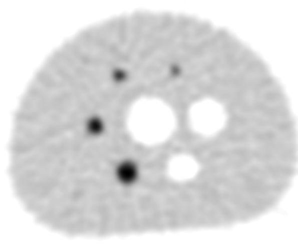

(c) URL_{sq}^4

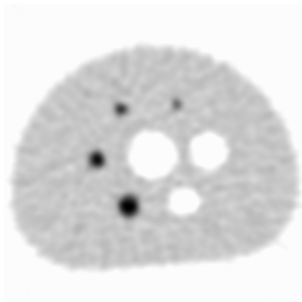

(d) URL_{hex}^4

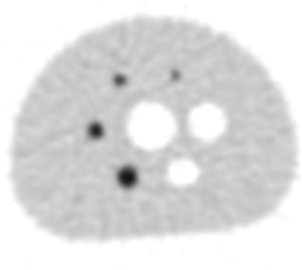

(e) USL^4

Figure 6.11: Upsampled results for NEMA phantom

6.5 Hoffman Brain Phantom

The Hoffman phantom was used mainly to study the effect of up-sampling on the quality of image in terms of noise content and contrast. This phantom was used to compare S, URL_{hex} and USL images. Out of 91 slices in the phantom, 2 slices i.e. the 19th and 24th are reconstructed. Figure 6.15 shows the up-sampled (by 4) images of the 24th slice of the Hoffman phantom and their corresponding amplitude spectra. The distribution for URL_{hex} is smoother as compared to S and USL, which means that URL_{hex} is able to suppress imaging when compared with S and USL. In contrast, the distribution for S and USL shows prominent variations which signifies presence of imaging.

Figure 6.16 (b) shows a line profile in the upsampled images, for a selected line in Figure 6.16 (a). To enable noting the difference in upsampled images, Table 6.2 shows the gray value difference (USL-S and URL_{hex}-S), in selected regions of these profiles: a trough region and

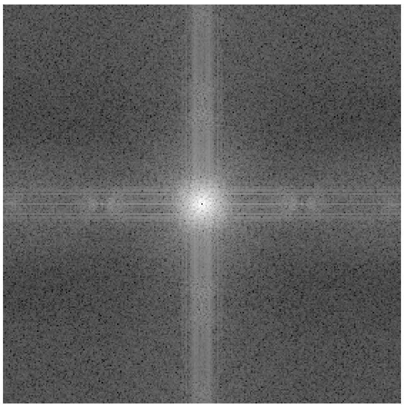

(a) S^4

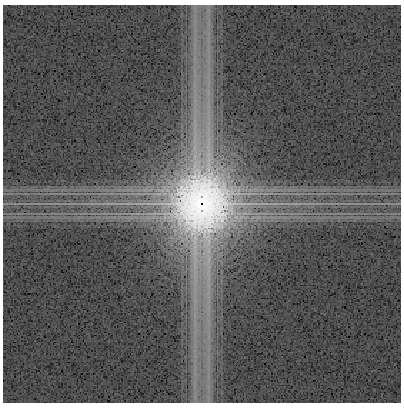

(b) H^4

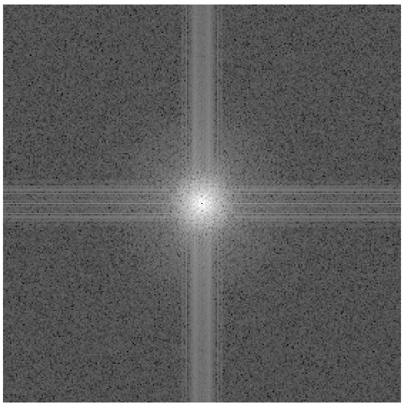

(c) URL^4_{sq}

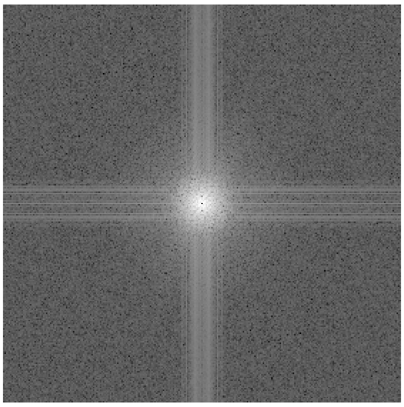

(d) URL^4_{hex}

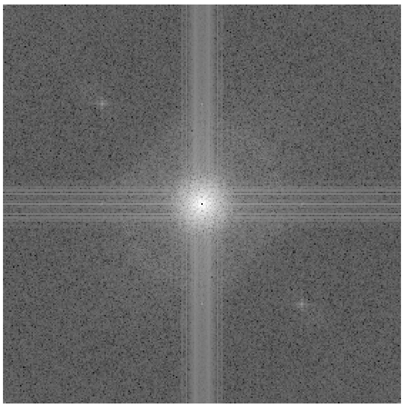

(e) USL^4

Figure 6.12: Corresponding full amplitude spectra of NEMA phantom.

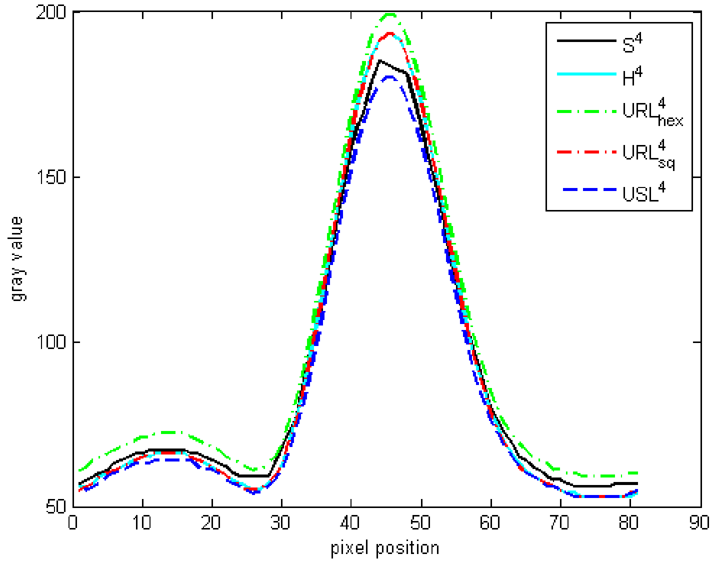

Figure 6.13: Radial line profiles of the smallest sphere in the NEMA phantom

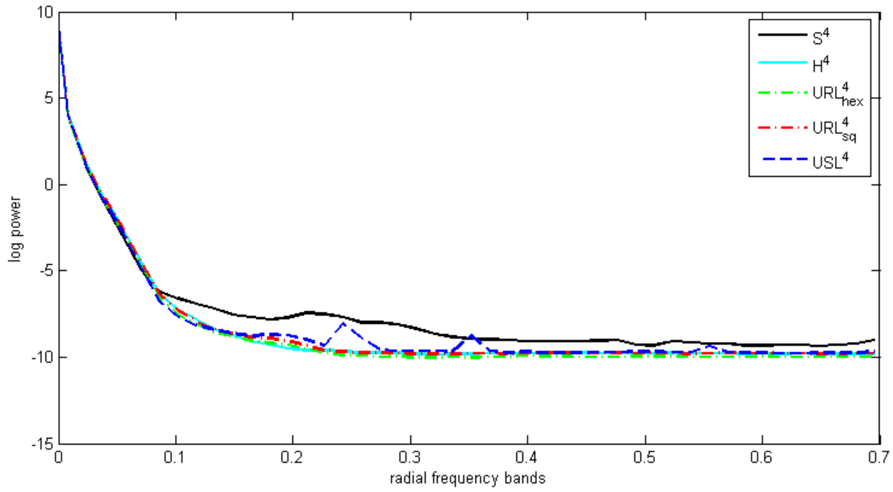

Figure 6.14: Radial energy plot of NEMA phantom for different upsampling methods

a crest region. For contrast enhancement the values should be positive for crest region and negative for trough region. Improvement in contrast (over S) in USL and URL images can be noted clearly from the average difference shown in this table. Since upsampling can introduce noise, we studied a noisy ROI. Figure 6.17 (a) shows a ROI of size 41×41 reconstructed from original sinogram (with no smoothing) of the 19th slice. The DC suppressed noise spectra

(a) S^4

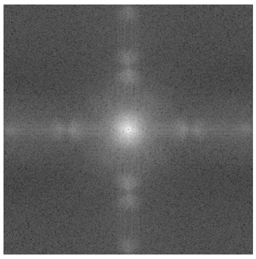

(b) S^4

(c) URL^4_{hex}

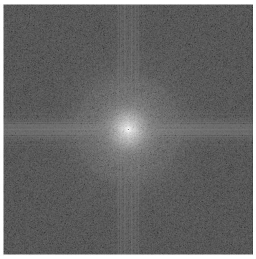

(d) URL^4_{hex}

(e) USL^4

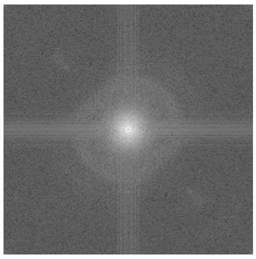

(f) USL^4

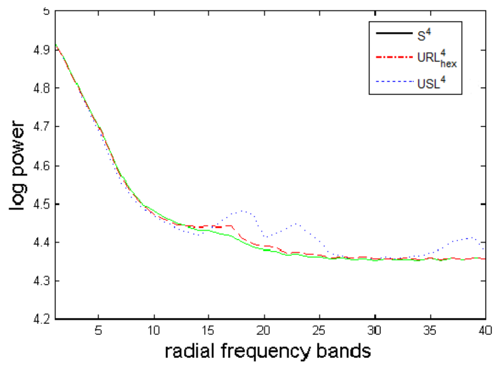

(g) energy plot

Figure 6.15: Upsampled results of 24th slice of Hoffman phantom and their corresponding amplitude spectras.(g) Energy plot of S^4,URL^4 and USL^4

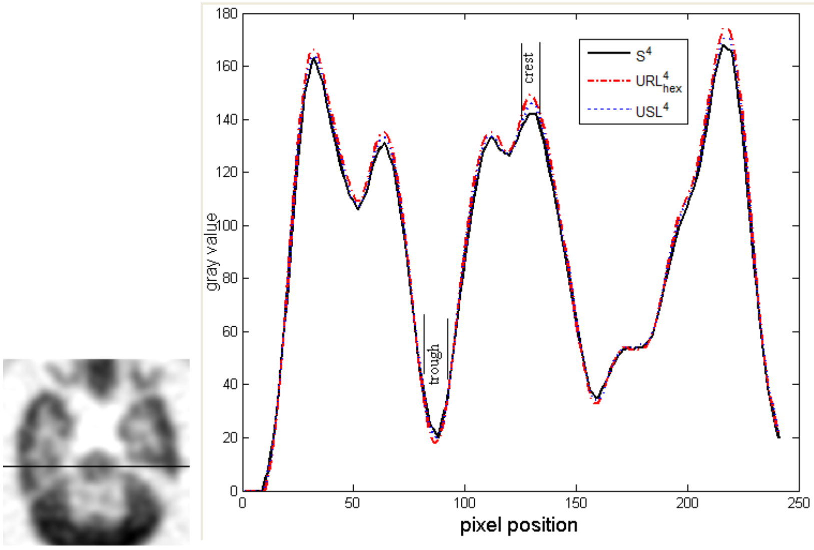

(a) selected line (b) line profile

Figure 6.16: Line profile of S^4,URL^4_{hex} and USL^4 of 24th slice of Hoffman phantom

Table 6.2: Difference in gray values of marked region 1 and 2 in 8(b)

Images	Difference in gray values of trough region											Avg
R-S	-2	-2	-3	-2	-4	-5	-3	-1	-2	-3	-1	-2.5
SR-S	-1	-1	-2	0	-2	-2	-1	+1	0	-2	-1	-1.0
Images	Difference in gray values of crest region											Avg
R-S	+5	+7	+7	+7	+7	+6	+4	+5	+5	+5	+5	5.7
SR-S	+2	+3	+3	+3	+4	+4	+3	+3	+3	+3	+2	3.0

for S^2, URL^2_{hex} and USL^2 images in Figure 6.17 (b) to (d) show that the noise content in URL^2_{hex} and USL^2 is circularly symmetric unlike S which is of wider bandwidth as well.

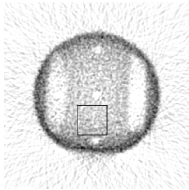

(a) ROI

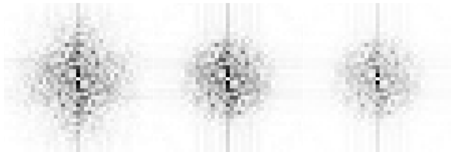

(b) S^2 (c) URL^2_{hex} (d) ${}^{U}SL^2$

Figure 6.17: (a) Shows ROI of 19th slice of Hoffman phantom used for computing noise spectra , (b),(c) and (d) Noise spectra of the ROI

6.6 Summary

In this chapter we have discussed two methods for generating upsampled images:

a)**Hexagonal lattice(single lattice)**: Results of the method were compared against direct up-sampled images (S). For concentric rings and NEMA, radial line plot illustrates a smooth variation for H as compare to S. Visually H is able to preserve the curved structure and line definition for concentric rings and lines phantom. However line profiles for dots phantom indicate that contrast of S is better than H.

b)**Super resolution(multiple lattice)**: The results of the method were compared against ISR-2 algorithm [17] and direct up-sampling. Visually for k=6 URL and USL images in Figure 6.10 appear to be same. The USL image was generated by combining 6 shifted images where as the URL image was generated by combining 2 rotated images. From analysis of line profile and contrast ratio, we can conclude that URL generates comparable quality image as USL and decreases the computational cost. Upsampled URL and USL images of concentric circles and dots preserve the definition of curves and dots compared to S; but for lines phantom, USL introduces prominent distortion in the vertical line. The radial energy distribution plot for concentric rings, Nema and Hoffman illustrates a smooth variation for URL and USL images. In contrast, the energy distribution of the S image has prominent irregularities beyond the baseband, thus indicating presence of imaging. From the spectra plots it is evident that URL suppresses imaging uniformly in all the directions. Where as, imaging suppression for USL is not uniform. Our purpose is to improve the quality of zoomed images by combining low resolution images which are rotated version of each other. Visually, the up-sampled images S, USL and URL for both NEMA and Hoffman phantoms appear to be the same. However, line profiles indicate contrast improvement. From the line profiles of both the phantoms it can also be concluded that the contrast of URL and USL is better than S. It is evident from the noise spectra of Hoffman phantom that rotated lattices and union of shifted lattices reduce the background noise relative to S. From the results it can be concluded that URL shows qualitative and quantitative improvement over direct upsampling but when compared with USL, generated upsampled images are of comparable quality.

Chapter 7

Conclusion and Future Work

Improving resolution of tomographic images is an active area of research in image processing. The usual size of CT and PET images is $512 \times 512 \times m$ and $128 \times 128 \times m$ respectively, where m is the number of slices. Medical images are typically zoomed or upsampled to observe the details for diagnosis. However, such transformations result in a deterioration and loss of information in the upsampled image and may lead to mis-diagnosis. Hence, preserving details and quality in an upsampled tomographic image is a challenge. In this thesis we have proposed two methods to improve the quality of upsampled images: 1) Single lattice and 2) Multiple lattice approach

Hexagonal lattice has been explored in generating tomographic images. In the single lattice approach, we proposed to extend the use of hexagonal lattice for generating upsampled tomographic images. Upsampled image (H) was generated by interpolating the samples defined on hexagonal lattice. Results of the proposed method were compared against direct up-sampled images (S), which is generated by interpolating samples defined on square lattice. From the results it is evident that H and S upsampled images are of similar quality. We can conclude that for generating upsampled images we can opt for hexagonal lattice instead of square because as discussed in Chapter 3, hexagonal sampling has an advantage over square sampling in terms of computation cost, better representation of signal, additional equi-distance neighbor and better representation of curved structures.

The proposed multiple lattice method is based on the concept of super-resolution. High resolution image is generated by combining *two* or more low resolution images. Low resolution images can be generated by translation or rotation. We examined the rotation alternative for generating upsampled tomographic images by combining samples from *two* low resolution images which are rotated versions of each other. These low resolution images are defined on square or hexagonal lattice and are derived from the same sinogram data. For validation, the results (union of rotated lattices:URL) of the proposed method were compared against ISR-2 (incomplete super resolution) algorithm (Union of rotated lattice: USL) [17] and direct up sampling (S). Results show that our scheme produced an image of better quality when compared with direct up-sampling method as well as of comparable quality to the image obtained with ISR-2 algorithm. Theoretically, for generating k times upsampled image k^2 shifted images are needed. ISR-1 and ISR-2 are two optimization techniques which require $2 \times (k-1)$ and k images respectively without affecting the quality of up-sampled images. Our proposed method offers further reduction as only two images are needed for any up-sampling (k=2...6) factor. This amounts to considerable savings in computational cost and storage space.

Both the above stated methods generate better quality image when compared to their conventional counterparts. We have used non-uniform splines in both the methods for generating the images. As part of the future work, different interpolation kernels like hex splines, b-splines etc should be explored for upsamplng. We also want to come up with a new adaptive kernel which will adapt according to density of sample points in multiple lattice approach. In case of Super resolution method we generated $URL_{sq}(URL_{hex})$ by combining images defined on rotated square lattice (hexagonal lattice) rotated by an angle 45° (60°). The angle value was experimentally chosen to get sparsely distributed samples. But ideally, angle should be chosen theoritically, which will give better cancellation of imaging. We also would like to explore the use of GPU platforms to generate upsampled images. We argue that using low resolution images≥ 2 in our proposed methods on a multicore architecture platform may enhace the image quality without generation time overhead.

7.1 Publications arising from this thesis

a)N. Dixit, N. V. K. Medathati, J. Sivaswamy, "Synthetic Zooming of Tomographic Images by Combination of Lattices", in *Nuclear Science Symposium Medical Imaging Conference*, Orlando, 2009, IEEE.

b)Neha Dixit and Jayanthi Sivaswamy, "Novel Approach to Generate Up-sampled Tomographic Images using Combination of Rotated Hexagonal Lattices", in *National Conference on Communication*, Chennai, 2010.

Chapter 8

Appendix A

We wish to examine the effect of combining samples from 2 rotated lattices in the fourier space. Conventional fourier transform of a continuous 2-D complex valued function $f(x,y)$ on cartesian coordinate is given as

$$F(X,Y) = \int_{-\infty}^{+\infty}\int_{-\infty}^{+\infty} f(x,y)e^{-2\pi i(xX+yY)}dxdy \tag{8.1}$$

Substituting $r = \sqrt{x^2+y^2}$ and $\theta = arctan(y/x)$, eqn8.1 becomes

$$F(X,Y) = \int_{0}^{2\pi}\int_{0}^{+\infty} f(r,\theta)e^{-i2\pi r(X\cos\theta+Y\sin\theta)}rdrd\theta \tag{8.2}$$

where $0 \le \theta \le 2\pi$ and $0 <= r < \infty$ Substituting $R = \sqrt{X^2+Y^2}$ and $\Theta = arctan(Y/X)$ in eqn.8.2

$$F(X,Y) = F(R,\Theta) \tag{8.3}$$

$$= \int_{0}^{2\pi}\int_{0}^{+\infty} f(r,\theta)e^{-i2\pi rR(\cos\Theta\cos\theta+\sin\Theta\sin\theta)}rdrd\theta \tag{8.4}$$

$$= \int_{0}^{2\pi}\int_{0}^{+\infty} f(r,\theta)e^{-i2\pi rR\cos(\theta-\Theta)}rdrd\theta \tag{8.5}$$

Next, we substitute the following relation in eqn.8.3

$$e^{iu\cos\phi} = \sum\nolimits_{n=0}^{\infty} i^n J_n(u)e^(in\phi) \tag{8.6}$$

where J_n is the Bessel function of order n, taking $u = 2\pi rR$ and $\phi = \theta - \Theta$, we derive [8]

$$F(R,\Theta) = \int_0^{2\pi}\int_0^{+\infty}\sum_{n=-\infty}^{\infty} f(r,\theta)i^n J_n(2\pi rR)e^{in(\theta-\Theta)}rdrd\theta \tag{8.7}$$

rearranging the above equation

$$F(R,\Theta) = \sum_{n=-\infty}^{\infty}[\int_0^{+\infty}(\int_0^{2\pi} f(r,\theta)e^{in\theta}d\theta)J_n(2\pi rR)rdr]i^n e^{-in\Theta} \tag{8.8}$$

$$= \sum_{n=-\infty}^{\infty} I_n i^n \tag{8.9}$$

where $I_n = [\int_0^{+\infty}(\int_0^{2\pi} f(r,\theta)e^{in\theta}d\theta)J_n(2\pi rR)rdr]e^{-in\Theta}$

Now lets consider the coordinate system is rotated by an angle $\delta\theta$, eqn.8.3 will for such system will be :

$$F(R,\Theta+\delta\theta) = \int_0^{2\pi}\int_0^{+\infty} f(r,\theta)e^{-i2\pi rR\cos(\theta-\delta\theta-\Theta)}rdrd\theta \tag{8.10}$$

Once again expanding in terms of bessel function and rearranging the equation will give us

$$F(R,\Theta+\delta\theta) = \sum_{n=-\infty}^{\infty}[\int_0^{+\infty}(\int_0^{2\pi} f(r,\theta)e^{in\theta}d\theta)J_n(2\pi rR)rdr]i^n e^{-in\Theta}e^{-in\delta\theta} \tag{8.11}$$

$$= \sum_{n=-\infty}^{\infty} I_n i^n e^{-in\delta\theta} \tag{8.12}$$

Combining samples of 2 rotated lattices is the operation of interest. Hence adding eqn. 8.8 and 8.11

$$F(R,\Theta+\delta\theta) + F(R,\Theta) = \sum_{n=-\infty}^{\infty} I_n i^n + \sum_{n=-\infty}^{\infty} I_n i^n e^{-in\delta\theta} \quad = \sum_{n=-\infty}^{\infty} I_n i^n(1+e^{-in\delta\theta}) \tag{8.13}$$

Eqn.8.13, provides the guideline for choosing the angle between the two images which will give maximum cancellation of imaging and hence will preserve the details.

Chapter 9

Appendix B

In the given figure **??**, OP, OQ are axis of hexagonal coordinate and OR, OS are axis of hexagonal coordinate rotated by an angle θ with respect to OP and OQ. Point E is represented as (x,y) and (x',y') in OP, OQ and OR, OS coordinate systems respectively.

$$OA + AE" = OC" + C"E" \tag{9.1}$$

$$OA + AE" = OC" + C'E' \tag{9.2}$$

Substituting $OA = x$, $AE" = y\cos 60$, $OC" = x'\cos\phi$ and $C'E' = y'\cos(60+\theta)$, eqn9.1 becomes

$$x + y\cos 60 = c'\cos\phi + y'\cos(60+\phi) \tag{9.3}$$

Similarly we can write;

$$EE" = E'E" + EE' \tag{9.4}$$

$$EE" = C'C" + EE' \tag{9.5}$$

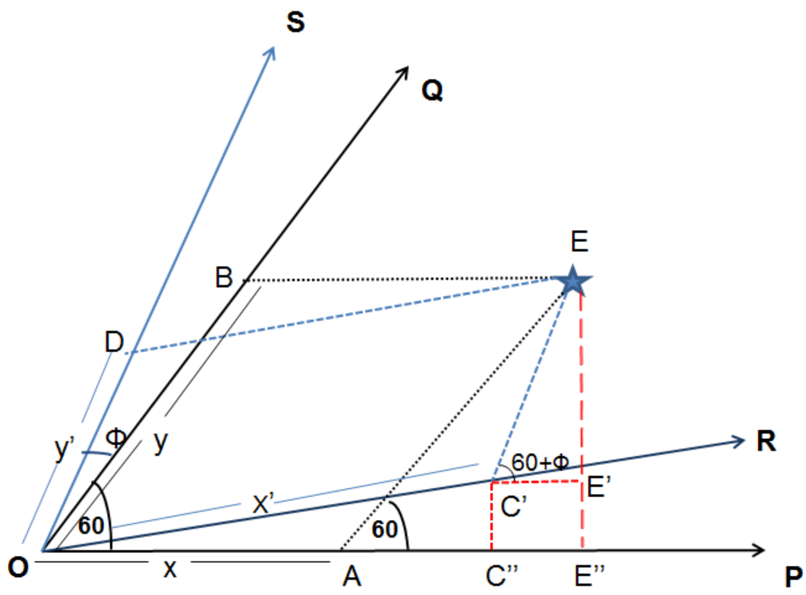

Figure 9.1: Hexagonal and rotated hexagonal coordinate

Substituting $EE" = y\sin 60$, $C'C" = x'\sin\phi$ and $EE' = y'\sin(60+\phi)$, eqn 9.4 becomes

$$y\sin 60 = x'\sin\phi + y'\sin(60+\phi) \tag{9.6}$$

solving 9.3 and 9.6 for x and y

$$\begin{bmatrix} r \\ s \end{bmatrix} = \frac{1}{\text{sin60}} \begin{bmatrix} \sin(60+\phi) & \sin\phi \\ -\sin\phi & \sin(60-\phi) \end{bmatrix} \begin{bmatrix} x \\ y \end{bmatrix} \tag{9.7}$$

$$\begin{bmatrix} x \\ y \end{bmatrix} = \frac{1}{\text{sin60}} \begin{bmatrix} \sin(60-\phi) & -\sin\phi \\ \sin\phi & \sin(60+\phi) \end{bmatrix} \begin{bmatrix} r \\ s \end{bmatrix} \tag{9.8}$$

Bibliography

[1] `http://www.biodex.com/nuclear-medicine/products/phantoms`.

[2] Ucsf ild program protocol for high-resolution ct scanning of the chest.

[3] A.Yabushita. Image reconstruction with hexagonal grid. In *Med Imagingtechnology*, volume 21, pages 239–245, 2003.

[4] S. Baker and T. Kanade. Limits on super-resolution and how to break them. In *IEEE Trans. Pattern Anal. Mach. Intell.*, volume 9, page 11671183, 2002.

[5] Guy M. Besson. Data rebinning to increase resolution in ct image reconstruction, June 2002.

[6] Charles L. Byrne. Accelerating the emml algorithm and related iterative algorithms by rescaled block-iterative methods. In *IEEE Trans. Image Processin*, volume 7, pages 100–109, 1998.

[7] Chen, Guang-hong, and Hsieh Jiang. Method for increasing the resolution of a ct image during image reconstruction, October 2009.

[8] Brian E. Coggins and Pei Zhou. Polar fourier transforms of radially sampled nmr data. In *Journal of Magnetic Resonance*, volume 182, pages 84–95, 2006.

[9] M. Dahlbom. Methods for improving image quality in whole boy pet scanning. In *IEEE Trans. Nucl. Med.*, volume 6, pages 1191–1199, 1992.

[10] M. Dahlbom. Characterization of sampling schemes for whole body pet imaging. In *IEEE Trans. Nucl. Sci.*, volume 41, pages 1571–1576, 1994.

[11] D.L.Snyder, M.I.Miller, L.J.Thomas, and D.G.Politte. Noise and edge artifacts in maximum-likelihood reconstructions for emission tomography. In *IEEE Trans. Med. Imag.*, volume 6, pages 228–238, 1987.

[12] J.A. Fessler. Image reconstruction toolbox. `http://www.eecs.umich.edu/fessler/code`.

[13] J.A. Fessler. Penalized weighted least-squares image reconstruction for positron emission tomography. In *IEEE Trans. Med. Imag*, volume 13, pages 290–300, 1994.

[14] J.A. Fessler and A.O. Hero. Space-alternating generalized expectation- maximization algorithm. In *IEEE Trans. Sig. Proc*, volume 42, pages 2664–2677, 1994.

[15] J.A. Fessler and A.O. Hero. Penalized maximum-likelihood image reconstruction using space-alternating generalized em algorithms. In *IEEE Trans. Image Proc.*, volume 4, pages 1417–1429, 1995.

[16] F.Faille and M.Petrou. Bio-inspired,invariant image reconstruction from irregularly placed samples. In *British Machine Vision Conference*, 2008.

[17] G.Chang, T.Pan, J.Clark, and OR Mawlawi. Optimization of super-resolution processing using incomplete image sets in pet imaging. In *Med. Phys*, volume 35, pages 5748–5757, 2008.

[18] G.Chang, T.Pan, J.Clark, and OR Mawlawi. Comparison between two super-resolution implementations in pet imaging. In *Med. Phys*, volume 36, pages 1370–1383, 2009.

[19] H.Behmard. Reconstruction of 2-d signals from union of shifted lattice. In *Proc. ICASSP*, volume 4, pages 197–120, 2005.

[20] H. M. Hudson and R. S. Larkin. Accelerated image reconstruction using ordered subsets of projection data. In *IEEE Trans. Med. Imag.*, volume 13, pages 601–609, 1994.

[21] B. R. Hunt. Super-resolution of images: Algorithms, principles, performance. In *Int. J. Imag. Syst. Technol.*, volume 6, pages 297–304, 1995.

[22] Anil K Jain. *Fundamentals of digital image processing.* Prentice-Hal, 1989.

[23] Jiri and Jan. *Medical image processing, reconstruction, and restoration, concepts and methods.* CRC Press, 2006.

[24] A. C. Kak and Malcolm Slaney. *Principles of Computerized Tomographic Imaging.* IEEE Press, 1988.

[25] John A. Kennedy. Super-resolution in pet imaging. In *IEEE Trans. On Med. Imag*, volume 25, pages 137–147, 2006.

[26] L.Middleton and J.Sivaswamy. *Hexagonal Image Processing: A Practical Approach.* New York: Springer, 2005.

[27] M.Knaup, S.Steckmann, O.Bockenbach, and M. Kachelrie. Ct image reconstruction using hexagonal grid. In *Nuclear science symposium*, volume 4, pages 3074–3076, 2007.

[28] E.U. Mumcuogln, R. Leahy, S.R. Cherry, and Z. Zhou. Fast gradient-based methods for bayesian reconstruction of transmission and emission pet images. In *IEEE Trans. Med. Imag.*, volume 13, pages 687–701, 1994.

[29] N.B. Nill and B.H. Bouzas. bjective image quality measure derived from digital image power spectra. In *Optical Engineering*, volume 31, pages 813–825,, 1992.

[30] John M. Ollinger and Jeffrey A. Fessler. Positron emission tomography. *IEEE SIGNAL PROCESSING MAGAZINE*, 14:43–55, Jan 1997.

[31] P.Vandewalle, K.Krichane, and P.Zbinden. Super resolution toolbox. `http://lcavwww.epfl.ch/software`.

[32] R.Mayers. The application of pet mr image registration in the brain. In *The British Journal of Radiology*, volume 75, pages s31–s35, 2002.

[33] R.M.Mersereau. The processing of hexagonally sampled two dimensional signals. In *IEEE Proc.*, volume 67, pages 930–949, 1979.

[34] K. Sauer and C. Boumau. A local update strategy for iterative reconstruction from projections. In *IEEE Trans. Sig. Proc.*, volume 41, pages 534–548, 1993.

[35] S.H.Izen, D.P.Rohler, and K.L.A. Sastry. Exploiting symmetry in fan beam ct: Overcoming third generation undersampling. In *SIAM J. Appl Math*, volume 65, pages 1027–1052, 2005.

[36] S.K.Kim, M.Allen-Auerbach, J.Goldin, B.J.Fueger, M.Dahlbom, M.Brown, J.Czernin, and C.Schiepers. Accuracy of pet/ct in characterization of solitary pulmonary lesions. In *J. Nucl. Med.*, volume 48, pages 214–220, 2007.

[37] R.C. Staunton and N. Storey. A comparison between square and hexagonal sampling methods for pipeline image processing. In *Proceedings of SPIE*, pages 142–151, 1989.

[38] Paul Sueten. *Fundamental of medical imaging*. Cambridge University Press, 2002.

[39] P. Vandewalle, S. Ssstrunk, and M. Vetterli. A frequency domain approach to registration of aliased images with application to super-resolution. In *EURASIP Journal on Applied Signal Processing (special issue on Super-resolution)*, volume 14, 2006.

[40] Y.Nie, Q.Li, F.Li, Y.Pu, D.Appelbaum, and K.Doi. Integrating pet and ct information to improve diagnostic accuracy for lung nodules:a semiautomatic computer-aided method. In *J. Nucl. Med.*, volume 47, pages 1075–1080, 2006.